

## Atomistic simulation of the mechanisms of noble gas incorporation in minerals

Z. Du <sup>a,b,c,\*</sup>, N.L. Allan <sup>a</sup>, J.D. Blundy <sup>b</sup>, J.A. Purton <sup>d</sup>, R.A. Brooker <sup>e</sup>

<sup>a</sup> School of Chemistry, University of Bristol, Cantocks Close, Bristol BS8 1TS, UK

<sup>b</sup> CETSEI, Department of Earth Sciences, University of Bristol, Wills Memorial Building, Bristol BS8 1RJ, UK

<sup>c</sup> Department of Chemistry, University College London, 20 Gordon Street, London WC1H 0AJ, UK

<sup>d</sup> CLRC, Daresbury Laboratory, Warrington, Cheshire WA4 4AD, UK

<sup>e</sup> Department of Earth Sciences, University College London, London WC1E 6BT, UK

Received 30 May 2007; accepted in revised form 4 October 2007; available online 13 October 2007

### Abstract

Atomistic simulations have been carried out to investigate the mechanisms of noble gas incorporation in minerals using both the traditional two-region approach and the “supercell” method. The traditional two-region approach has been used to calculate defect energies for Ne, Ar, Kr and Xe incorporation in MgO, CaO, diopside and forsterite in the static limit and at one atmosphere pressure. The possibilities of noble gas incorporation via both substitution and interstitial mechanisms are studied. The favored mechanism varies from mineral to mineral and from noble gas to noble gas. In all minerals studied, the variation of the solution energies of noble gas substitution with atomic radius appears approximately parabolic, analogous to those for 1<sup>+</sup>, 2<sup>+</sup>, 3<sup>+</sup> and 4<sup>+</sup> trace element incorporation on crystal lattice sites. Noble gas solution energies thus also fall on a curve, similar to those previously observed for cations with different charges, but with much lower curvature.

The “supercell” method has been used to investigate the pressure dependence of noble gas incorporation in the same systems. Results indicate a large variation of the solubility of the larger noble gases, Kr and Xe with pressure. In addition, explicit simulation of incorporation at the (001) surface of MgO shows that the solubility of the heavier noble gases may be considerably enhanced by the presence of interfaces.

© 2007 Elsevier Ltd. All rights reserved.

### 1. INTRODUCTION

The understanding of the partitioning of trace elements between minerals and melts is crucial to many geochemical processes. Incorporation and partitioning behaviour of noble gases in particular is important to understand a wide range of planetary processes from accretion to mantle dynamics and the formation of atmosphere (Allègre et al., 1987; Turner, 1989; Allègre et al., 1996; Harper and Jacobson, 1996). The concentration of noble gases in the Earth is about 10<sup>-9</sup>–10<sup>-1</sup> ppm by weight. Noble gases and their isotopes were originally incorporated in the Earth when it

formed, were added by subsequent cometary impacts, or have been produced subsequently by radioactive decay (Jambon, 1997). By virtue of the existence of both radiogenic (e.g., <sup>4</sup>He from U, Th decay, <sup>40</sup>Ar from <sup>40</sup>K decay, <sup>129</sup>Xe from <sup>129</sup>I) and non-radiogenic (primordial) isotopes (e.g., <sup>3</sup>He, <sup>36</sup>Ar and <sup>132</sup>Xe), noble gases can, in principle, be used to constrain the processes of earth differentiation and to decipher mantle structure and constrain the number and size of terrestrial geochemical reservoirs. The inert chemical behaviour of the noble gases makes them excellent tracers in geochemistry. Thus it is generally considered that noble gases behave as perfectly incompatible (mineral–melt partition coefficient,  $D \approx 0$ ), volatile trace elements during mantle melting and on magma eruption or crystallisation they are degassed extensively to atmosphere. Partition coefficients and solubility of noble gases in key minerals are

\* Corresponding author. Fax: +44 207631 6803.  
E-mail address: [z.du@ucl.ac.uk](mailto:z.du@ucl.ac.uk) (Z. Du).

thus fundamental parameters needed for an understanding of the early history of the Earth and its present day degassing.

Much effort has been devoted over the last few decades to investigate the behaviour of noble gases dissolved in various minerals and melts of geochemical interest (Hayatsu and Waboso, 1985; Jambon et al., 1986; Lux, 1987; Carroll, 1991; Carroll et al., 1993). However, quantitative experimental data are sparse, despite many advanced techniques used for experimental investigations. The understanding of the behaviour of noble gases in natural samples remains incomplete and many results are conflicting. Geochemists have traditionally considered the 'inert' noble gases as extremely incompatible elements with almost 100% extraction efficiency from the solid phase during melting processes. However some published experimental data on partitioning between crystalline silicates and melts has suggested that noble gases approach compatible behaviour and a significant proportion should remain in the residual solid mantle during extraction of silicate melts (Hiyagon and Ozima, 1986; Broadhurst et al., 1990, 1992; Carroll and Draper, 1994; Shibata et al., 1994). Hiyagon and Ozima (1986) concluded from their noble gas partitioning experiments on olivine/melt and diopside/melt systems that noble gases were somewhat incompatible ( $0.01 \leq D \leq 0.3$ ) and mineral–melt partition coefficients increased with increasing atomic number of noble gas. Broadhurst et al. (1992) reported an extensive series of partitioning experiments on anorthite, diopside, forsterite, spinel and synthetic basaltic. They also found that partition coefficients of noble gases increase with increasing atomic number but observed surprisingly high partition coefficients ( $0.01 \leq D \leq 47$ ). More recently, Brooker et al. (2003) and Heber et al. (2007) presented experimental data showing that noble gases are more incompatible than previously demonstrated, but not necessarily to the extent assumed or required by geochemical models. The models derived from limited noble gas data have often been at odds with available theories (O'Nions and Oxburgh, 1983; Van der Hilst et al., 1997; Van Keken and Ballentine, 1999). Virtually all earth evolution models have assumed that all noble gases are equally incompatible during melting/crystallization. However, there is evidence for differences between the different gases in terms of their geochemical behaviour. For instance, Honda and Patterson (1999) and Ozima and Igarashi (2000) show that the abundances of the primordial isotopes of Ar, Kr and Xe covary with one another in MORB and OIB, but Ne behaves slightly different and  $^3\text{He}$  abundances are not correlated at all with those of the other noble gases. Evidently, the ability to model noble gases during mantle melting is severely compromised by the ignorance of the mechanisms by which noble gas atoms are incorporated into crystals. There is a widespread view that, unlike trace cations which can clearly enter lattice sites, the 'inert' noble gases reside at extended defects, intrinsic defects or grain boundaries and are therefore not subject to the same thermodynamic controls on crystal–melt partitioning. There is so far no consistent view of how noble gases are incorporated into minerals and how noble gases partition between coexisting crystals and melts.

With the increase in computer power and developments in computational methodology, the problem of trace element and defect incorporation can now be tackled using a variety of modern computational techniques. Many theoretical studies of the incorporation of trace elements in a range of complex oxides and minerals have been carried out (Catlow and Mackrodt, 1982; Allan and Mackrodt, 1993; Purton et al., 1996, 1997). Purton et al. (1996) have successfully used calculated point-defect energies to estimate solution energies of homovalent cation substitution in a range of minerals (CaO, diopside, forsterite and enstatite). These calculations were later extended to heterovalent substituents (Purton et al., 1997). For heterovalent substituents, there are several additional complications due to the charge difference between the host cation and substituent trace element cation. Firstly, the polarization of the lattice resulting from a charged defect has to be taken into account. Secondly, the charged defect must be accompanied by a charge-compensating defect (or defects) to maintain charge balance. In the study of Purton et al. (1997) both substituent and possible compensating defects and their spatial arrangement were considered. In this paper, we further extend these ideas to the investigation of the incorporation of noble gases in minerals and their partitioning behaviour. In this paper, we do not attempt to calculate mineral–melt partitioning coefficients directly but focus on possible mechanisms of noble gas incorporation in minerals by means of classical atomistic simulations. Our methods are similar to those of Purton et al. (1996, 1997). The traditional two-region approach as well as the "supercell" approach have been used to calculate both defect energies and solution energies for noble gases occupying a lattice site as well as located at interstitial positions. A set of key minerals has been selected, including MgO, CaO, diopside ( $\text{CaMgSi}_2\text{O}_6$ ) and forsterite ( $\text{Mg}_2\text{SiO}_4$ ). Unlike zeolites, which have been subject to several previous studies (Smit and Siepmann, 1994; Watanabe et al., 1995; Vlucht et al., 1999), our chosen minerals are dense materials, which do not contain cavities where large atoms, such as noble gases, may accumulate. For such dense minerals, the powerful Grand Canonical Monte-Carlo simulation technique, which works well for calculating solubilities of gases in zeolites, become inefficient. The problem is that due to the high density of the minerals, the probability of successful insertion steps, which is a key step of the GCMC movement, becomes very small. In most cases, the insertion becomes impossible due to the constant overlap between the gas molecule and the atoms in the mineral. Some Monte-Carlo simulations in zeolites (Pellenq and Nicholson, 1995) have shown that the solubility of the noble gases increases in these materials with increasing atomic number. But is this still true for noble gas incorporation in other minerals?

Previous simulations of noble gases in minerals other than zeolites are almost non-existent. Tsuchiyama and Kawamura (1994) have performed molecular dynamics simulations of noble gases in MgO. These authors did not consider charge-compensating defects, which we discuss in detail below. Instead they explicitly introduced cation and anion vacancies into the crystal. Such defects are high in energy for MgO (e.g., Allan and Cooper (1987)). Nevertheless

they observed a rich variety of behaviour. Smaller noble gas atoms occupied interstitial sites, while larger atoms (Ar and Kr) occupied the vacancy positions.

## 2. THEORY, METHODS AND MODELS

Trace element incorporation into crystals involves interaction between these elements and the surrounding atoms. We use both the two-region approach and a “supercell” method for calculating defect energies. The two-region embedded defect(s) technique (Catlow and Mackrodt, 1982) has been widely used for study of doped systems of complex oxides and a variety of silicate minerals. One or more defects are introduced into the crystal. Initially, unrelaxed defect energies are calculated without allowing any atoms to move and then the total energy of the defective system is minimised by a relaxation of the positions of the atoms surrounding the defect to accommodate the misfit cations. The crystal is divided into an inner region, I, and an outer region, II (Fig. 1(a)). In the inner region, which immediately surrounds the point defect, the relaxation is assumed to be greatest and the elastic force equations solved explicitly. In the outer region, lattice relaxation is assumed to be much smaller and estimated using the Mott–Littleton approximation (Mott and Littleton, 1938). In the calculations reported here region I contains about 500 atoms for all the minerals studied, which is sufficient to ensure convergence of defect energy with the size of inner region. Final relaxed defect energies are obtained at minimisation. This technique is computationally cheaper but not readily generalized to finite temperatures and high pressures. The majority of point-defect calculations have assumed zero temperature and, for the most part, have involved the evaluation of the static part of the internal energy change accompanying defect information only at constant volume. Hence only the potential energy of the static lattice is evaluated and the vibrational contribution is neglected. The dependence of defect enthalpies on temperature is often small. Catlow et al. (1981), Allan et al. (1987) and Taylor et al. (1997) have given theoretical justification for this and some examples as well. It is therefore usually assumed that defect enthalpies ( $h_p$ ) at elevated temperatures are equal to the change in internal energy ( $u_v$ ) at 0 K ( $h_p(T) \approx u_v(0)$ ). This appears to be why calculated energies so often agree well with measured enthalpies.

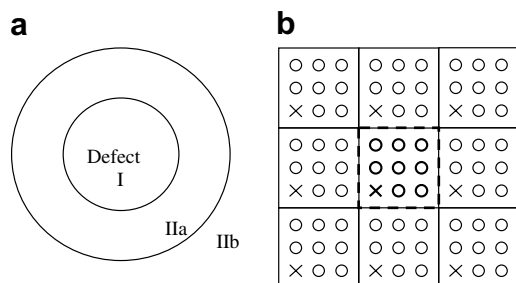


Fig. 1. Strategy of (a) the two-region and (b) the “supercell” method for defect energies.

At high pressure we have used the “supercell” method (Allan et al., 1987; Taylor et al., 1997) since embedding methods such as the Mott–Littleton approximation are not readily extended to such conditions (region I cannot be maintained at high pressure in the minimisation). The “supercell” approach is based on the direct minimisation, at a given external pressure, of the static or free energy of periodic solids with respect to the geometrical coordinates, possibly using very large unit cells. In this method, a “supercell” is constructed, which usually contains more than one primitive unit cell. One or more defects are then introduced into the ‘supercell’ such that it remains charge neutral. A superlattice of defects is thus produced which extends throughout the macroscopic crystal. The periodicity is that of the superlattice itself. The larger the supercell, the lower the defect concentration (Fig. 1(b)); there is convergence towards the properties of the isolated point-defect as the supercell size increases. The choice of size is a compromise between choosing a very large supercell so that the defects are far away from each other, minimising the interaction between defects, and the large amount of computer time needed for optimisations of the structures of large supercells. This technique is particularly useful for the direct evaluation of the defect enthalpies and entropies at elevated temperatures and/or high pressures.

For all defect energy calculations in this study, integer ionic charges are assigned to all ions based on accepted chemical valence and electron counting rules, *i.e.* 2+ for Ca and Mg, 4+ for Si, 2– for O and so on. A harmonic three-body bond-bending term is used for the O–Si–O interaction. The shell model of Dick and Overhauser (1958) is used to take the polarisation of  $O^{2-}$  into account. The  $O^{2-}$  ion consists of a massive core linked to a massless shell by a harmonic spring. The ionic charge is divided between the core and the shell such that the sum of their charge is the total ion charge (2–). All defect energy calculations conducted in this work are performed using the General Utility Lattice Program (Gale, 1997).

The success of any simulation relies on the accuracy of the interaction parameters. In our studies there are three different sets of interaction involved: gas–gas interaction, solid–solid interaction and gas–solid interaction. For solid–solid interaction, the cation–cation interaction is assumed to be purely Coulombic. Non-Coulombic cation–oxygen and oxygen–oxygen interactions are described by two-body potential functions of the Buckingham form. Thus for any pair,

$$U(r_{ij}) = \frac{q_i q_j}{4\pi\epsilon_0 r_{ij}} + A_{ij} \exp\left(-\frac{r_{ij}}{\rho_{ij}}\right) - \frac{C_{ij}}{r_{ij}^6} \quad (1)$$

where the first term on the right-hand side (RHS) is the Coulombic term handled by an Ewald sum (1921), and the second and the third RHS terms the short-range Buckingham potential, for which there is a well-established potential set available for a wide of range of silicate minerals (Sanders et al., 1984; Lewis and Catlow, 1985). The traditional way to test the accuracy of set of potentials is to compare the calculated structure with that from experiment. Purton et al. (1996) showed that, for example, the same potential set reproduced well the structures of CaO,

diopside and forsterite. We use this potential set in the current study, supplemented by a new set of potentials for the interactions between the noble gases and the silicate mineral. The derivation of the potentials involving the noble gases is not straightforward and is described in detail in [Appendix A](#). The complete set of interaction parameters used in this work is listed in [Table 1](#).

### 3. RESULTS AND DISCUSSION

#### 3.1. The mechanisms of noble gas incorporation in minerals

Unlike trace cations, for which incorporation behaviour in crystals as well as their partitioning behaviour is relatively well-understood, there is no consensus as to how noble gases are incorporated into crystal lattices, nor their partitioning behaviour. Do the noble gases enter a crystal lattice in just the same way as trace cation elements? Do they cause lattice strain due to their atomic size mismatch? To verify this, we have extended the methods described for trace element cations ([Purton et al., 1996, 1997](#)) to noble gases. Firstly the traditional two-region approach is used to obtain the defect energies as well as solution energies of noble gas incorporation in minerals in the static limit. The possibility of noble gas incorporation via both substitution and interstitial mechanisms is considered. Like heterovalent cations, the incorporation of a noble gas atom into a crystal is more complex than that of an isovalent cation. Substitution of a noble gas for a  $\text{Ca}^{2+}$  or  $\text{Mg}^{2+}$  ion gives rise to a charged defect. To ensure overall charge balance, charge-compensating defects must also be incorporated. Charge compensation produces overall two or more defects. These may either be isolated, i.e., so remote from each other that the total defect energy is the sum of energies of the isolated defects, i.e.,  $E(M^0) + E(M^{4+})$ , or they may be situated close to one another. If the latter, there is then an association energy between defects with effective opposite charges. The energy for the defect complex, denoted as  $E(M^0 + M^{4+})$ , will be lower than  $E(M^0) + E(M^{4+})$  ([Purton et al., 1997](#)). A simple calculation of the interaction between two point charges separated by  $\sim 3 \text{ \AA}$  (the M1–M1 distance in diopside and forsterite) in a continuum with a dielectric constant set equal to that of a typical silicate mineral shows that the effect of association is large. For example, formation energies for  $E(M^{3+} + M^+)$  are lower by  $\sim 100 \text{ kJ mol}^{-1}$  than  $E(M^{3+}) + E(M^+)$  ([Purton et al., 1997](#)). In this study we have therefore considered only associated defects.

As in [Purton et al. \(1997\)](#), a range of plausible associated charge-compensating defects has been investigated to identify the lowest energy mode for noble gas substitution. In diopside and forsterite it has been found, consistent with results for alkali metal incorporation ([Purton et al., 1997](#)), that two  $\text{Sc}^{3+}$  at adjacent cation M1 sites gives the lowest solution energies for noble gas substitution. In CaO and MgO, there is only one substitution site, and here two  $\text{Sc}^{3+}$  are simply placed at adjacent cation positions. All the results for noble gases presented in this paper are based on this charge-compensating combination. We stress that additional studies have shown that the *variation* of solution

Table 1  
Interatomic potential models used in this work

Inter-molecular	$A$ (eV)	$\rho$ ( $\text{\AA}$ )	$C$ ( $\text{eV \AA}^6$ )
<i>Buckingham potential (Eq. (1))</i>			
$\text{Si}^{4+}\text{-O}^{2-}$	1283.91	0.32052	10.66
$\text{O}^{2-}\text{-O}^{2-}$	22764.00	0.14900	27.88
$\text{Al}^{3+}\text{-O}^{2-}$	1114.90	0.3118	0.00
$\text{Na}^+\text{-O}^{2-}$	1266.84	0.3065	0.00
$\text{Ca}^{2+}\text{-O}^{2-}$	1090.39	0.3437	0.00
$\text{Mg}^{2+}\text{-O}^{2-}$	1428.50	0.2945	0.00
$\text{Sc}^{3+}\text{-O}^{2-}$	1299.39	0.3312	0.00
$\text{Zr}^{4+}\text{-O}^{2-}$	1453.80	0.3500	0.00
	$A$ ( $\text{eV \AA}^{12}$ )		$B$ ( $\text{eV \AA}^6$ )
<i>Lennard-Jones potential (Eq. (10))</i>			
Ne–Ne	2736.1740		5.8012
Ar–Ar	100166.9860		64.2720
Kr–Kr	640600.9453		184.8800
Xe–Xe	2633133.2634		440.5703
Ne– $\text{Si}^{4+}$	4.6767		0.1723
Ne– $\text{Al}^{3+}$	14.3029		0.3013
Ne– $\text{O}^{2-}$	3857.3231		8.9350
Ne– $\text{Mg}^{2+}$	231.2189		3.0225
Ne– $\text{Ca}^{2+}$	767.5165		5.5069
Ne– $\text{Sc}^{3+}$	264.3189		3.2316
Ne– $\text{Na}^+$	1045.8390		7.6833
Ne– $\text{Zr}^{4+}$	231.2189		3.0225
Ar– $\text{Si}^{4+}$	60.7666		0.8405
Ar– $\text{Al}^{3+}$	158.0652		1.3556
Ar– $\text{O}^{2-}$	25209.6201		30.9095
Ar– $\text{Mg}^{2+}$	2247.4736		12.7517
Ar– $\text{Ca}^{2+}$	6426.3266		21.5627
Ar– $\text{Sc}^{3+}$	2525.1680		13.5165
Ar– $\text{Na}^+$	8806.1512		30.1693
Ar– $\text{Zr}^{4+}$	2247.4736		12.7517
Kr– $\text{Si}^{4+}$	265.879283		1.875086
Kr– $\text{Al}^{3+}$	627.0524		2.8795
Kr– $\text{O}^{2-}$	71676.8747		55.5861
Kr– $\text{Mg}^{2+}$	8236.9387		26.0359
Kr– $\text{Ca}^{2+}$	21443.2511		42.0083
Kr– $\text{Sc}^{3+}$	9155.4955		27.4493
Kr– $\text{Na}^+$	29489.4873		58.8809
Kr– $\text{Zr}^{4+}$	8236.9387		26.0359
Xe– $\text{Si}^{4+}$	795.8733		3.5171
Xe– $\text{Al}^{3+}$	1763.7751		5.2359
Xe– $\text{O}^{2-}$	162143.3321		90.6396
Xe– $\text{Mg}^{2+}$	22019.0150		46.1509
Xe– $\text{Ca}^{2+}$	53929.1016		72.2259
Xe– $\text{Sc}^{3+}$	24304.5504		48.4870
Xe– $\text{Na}^+$	74338.9278		101.3540
Xe– $\text{Zr}^{4+}$	22019.0150		46.1509
	$k$ ( $\text{eV rad}^{-2}$ )		$\Theta_0$
<i>Three-body potential</i>			
$\text{O}^{2-}\text{-Si-O}^{2-}$	2.09724		109.470000

Integral ionic charges are assigned to all ions based on accepted chemical valence and electron counting rules, i.e., 2+ for Ca and Mg, 4+ for Si, 2– for O and so on. A shell model was used for the oxygen ions, with core charge  $0.86902e$ , shell charge  $-2.86902e$ , and spring constant  $74.9235 \text{ eV \AA}^{-2}$ . For the Lennard-Jones potential, parameters  $A$  and  $B$  stand for  $4\epsilon\sigma^{12}$  and  $4\epsilon\sigma^6$ , respectively, where  $\epsilon$  and  $\sigma$  are the Lennard-Jones interaction parameters indicated in [Appendix A](#) (Eq. (10)).

energy with noble gas atomic number remains basically the same whatever the charge-compensating defect (e.g., other two 3+ ions such as Al<sup>3+</sup> or Ho<sup>3+</sup> or one 4+ ion such as Zr<sup>4+</sup> or Ti<sup>4+</sup>). This is discussed further in Section 3.1.2.

In geochemical studies, partitioning is often related to the atomic or ionic radius of the substituent. For presentation purposes and the discussion of trends, we use the appropriate ionic or atomic radius. For diopside we have used the values for sixfold and eightfold coordinate radii (Shannon, 1976; Zhang and Xu, 1995) for all substitutions at the M1 site (Mg) and M2 site (Ca), respectively, whereas in forsterite both M1 and M2 are sixfold coordinate. It must be stressed that the simulations themselves do not involve in any way the use of atomic radii.

### 3.1.1. Defect and relaxation energies of noble gas substitution in minerals

We first present calculated defect energies (compensated by two Sc<sup>3+</sup>) for noble gas substitution in MgO, CaO, diopside (see e.g., Eq. (3)) and forsterite at zero pressure and these are collected together in Table 2. Both initial (unrelaxed),  $U_i$  and final (relaxed),  $U_f$  energies are given. The difference between the two, the relaxation energy ( $U_{rel} = (U_i - U_f)$ ), is also listed. Fig. 2 shows the variation of the relaxed defect energies with noble gas atomic radius for all minerals involved in this study. In every case the final relaxed defect energy ( $U_f$ ) increases with increasing noble gas atomic radius. All final relaxed defect energies are negative. This does not mean that the overall solution energies for noble gas substitution in these minerals are negative since these are a function not only of the defect energies but also the lattice energies of the binary oxides involved in the substitution reaction (Purton et al., 1996, 1997). Further details are given in the next section. The relaxed defect energies of noble gases in diopside (see Fig. 2(c)) show that the defect energies at the M2 site (Ca site) are lower than those at the M1 site (Mg), in agreement with the relative size of the two sites.

The relaxation energy is the energy released when the atoms move from their perfect lattice positions to accommodate the incoming trace element. The greater the relaxation energy, the larger is the mismatch between host and substituent. The relaxation energy is always a positive quantity. In Fig. 3, we have plotted the variation of calculated relaxation energy against the noble gas atomic radius. The figure shows that the general characteristics of these plots are similar for Mg sites in all the minerals studied, and similar also for all the Ca sites, which suggests that the rigidity of the local environment rather than that of the bulk crystal largely determines the relaxation energy. On both Ca and Mg sites, the relaxation energies exhibit an approximately parabolic dependence on the noble gas atomic radius. The curvature of the parabola is larger at the Mg sites than the Ca sites. Relaxation energies for the Mg site are more sensitive to substituent size. The minimum relaxation energy for the noble gases is a radius somewhat from that of the host atom (i.e., Mg in the M1 site and Ca in the M2 site of diopside), unlike for isovalent substitution (Purton et al., 1996).

In previous studies (Purton et al., 1996, 1997; Van Westrenen et al., 2000), the Brice lattice strain model (Brice, 1975) was adapted to describe successfully the near-para-

Table 2

Calculated initial defect energies (no relaxation) (IDE), final defect energies (including relaxation) (FDE), relaxation energies (RE) and solution energies (SE) for noble gas impurities in MgO, CaO, diopside and forsterite via the lattice site substitution mechanism

Impurity	IDE	FDE	RE	SE
<i>MgO</i>				
Ne	-537	-1710	1173	348
Ar	977	-1455	2432	603
Kr	4464	-1078	5542	980
Xe	11366	-621	11987	1437
<i>CaO</i>				
Ne	-1977	-3327	1349	285
Ar	-1727	-3282	1554	330
Kr	-1094	-3169	2075	442
Xe	-190	-3002	2812	609
<i>Diopside (M1 site)</i>				
Ne	-484	-1688	1204	374
Ar	646	-1569	2216	489
Kr	3265	-1405	4671	652
Xe	8452	-1222	9675	835
<i>Diopside (M2 site)</i>				
Ne	-1450	-2283	833	293
Ar	-1311	-2247	936	329
Kr	-930	-2152	1222	424
Xe	-143	-2008	1865	568
<i>Forsterite (M1 site)</i>				
Ne	-717	-1828	1111	230
Ar	551	-1695	2246	363
Kr	3476	-1519	4996	538
Xe	9266	-1316	10582	742
<i>Forsterite (M2 site)</i>				
Ne	-329	-1650	1321	409
Ar	703	-1543	2246	515
Kr	3095	-1396	4492	662
Xe	7838	-1321	9159	737

Oxide	MgO	CaO	Sc <sub>2</sub> O <sub>3</sub>
Lattice energy	-3986	-3468	-14016
Noble gas	Atomic radius <sup>a</sup> (sixfold)	Atomic radius <sup>a</sup> (eightfold)	
Ne	1.21	1.32	
Ar	1.64	1.77	
Kr	1.78	1.87	
Xe	1.96	2.03	

The lattice energies of the binary oxides used to calculate the solution energies are also listed as are the atomic radii (Zhang and Xu, 1995) of the noble gases. All results are for associated defects as described in the text. Energies are in kJ/mol and atomic radii are in Å.

bolic dependence of lattice strain energy on atomic radius. In this model, strain around a misfit element in an isotropic perfectly elastic crystal lattice is obtained using macroscopic strain theory and the strain energy per mole of trace element is given by

$$U = 4\pi E_z N_A \left[ \frac{r_o}{2} (r_M - r_o)^2 + \frac{1}{3} (r_M - r_o)^3 \right] \quad (2)$$

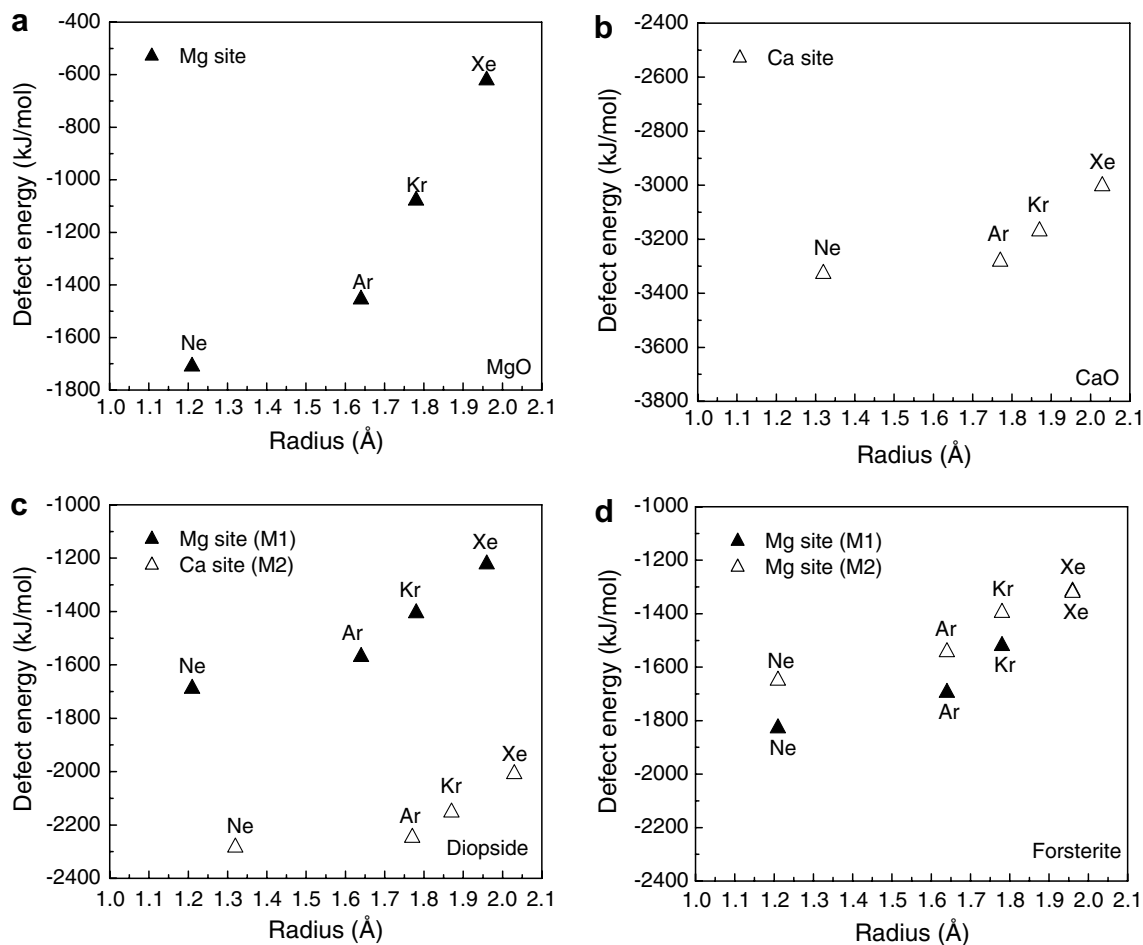


Fig. 2. Variation of defect energies for noble gas substitution in (a) MgO, (b) CaO, (c) diopside and (d) forsterite with atomic radius.

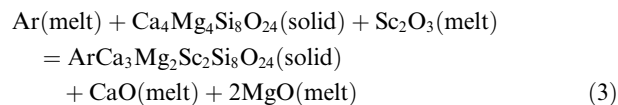
$E_x$  is the apparent Young's modulus of the site.  $r_M$  is the radius of the trace element and  $r_o$  is the optimum radius of the site.  $N_A$  is Avogadro's constant. We have fitted our series of relaxation energy values to the Brice model, i.e., to the RHS of Eq. (2) and these are shown as the curves in Fig. 3. Fitted values of apparent site Young's modulus  $E_x$  and the optimum radius of the site,  $r_o$ , for noble gas substitution are given in Table 3. It is clear that both  $E_x$  and  $r_o$  are broadly similar for similar sites in the minerals consistent with the relative compressibility of a site being dependent largely on the type of site and not the mineral in which the site occurs.

We stress that the defect energies and the relaxation energies themselves are only parts of the overall physical process involved in trace element partitioning. They are purely a solid-state property and ignore the presence of a melt phase.

### 3.1.2. Solution energies of noble gas incorporation via a substitution mechanism

In general, partitioning of noble gases between minerals and melts consists of three steps (i) removal of a noble gas from the melt, (ii) incorporation of the gas molecule into the mineral by a substitution mechanism and (iii) insertion

of the host cation(s), in our case either Mg or Ca, into the melt. Thus the melt must also play a role in noble gas partitioning. Here, as previously (Purton et al., 1997; Van Westrenen et al., 2000; Allan et al., 2001), we use an exchange reaction to describe approximately the partitioning process, and assume the noble gases behave ideally in the melt. An example is given below, in which argon substitutes for Ca (at the M2 site) with charge compensation of two  $\text{Sc}^{3+}$  at adjacent Mg site (M1 site):



The energy associated with this reaction is thus

$$E_{\text{sol}} = E_{\text{def}} + E_{\text{lat}}(\text{CaO}) + 2E_{\text{lat}}(\text{MgO}) - E_{\text{lat}}(\text{Sc}_2\text{O}_3) \quad (4)$$

$E_{\text{sol}}$  is the solution energy and  $E_{\text{lat}}$  is the lattice energy of the relevant binary oxide. As an approximation, following Purton et al. (1996, 1997) and Van Westrenen et al. (2000), we assume that the local environments of host and substituent trace elements in the melt are equivalent to their environments in the corresponding binary solid oxides. Hence the energy associated with the exchange reaction, the *solution*

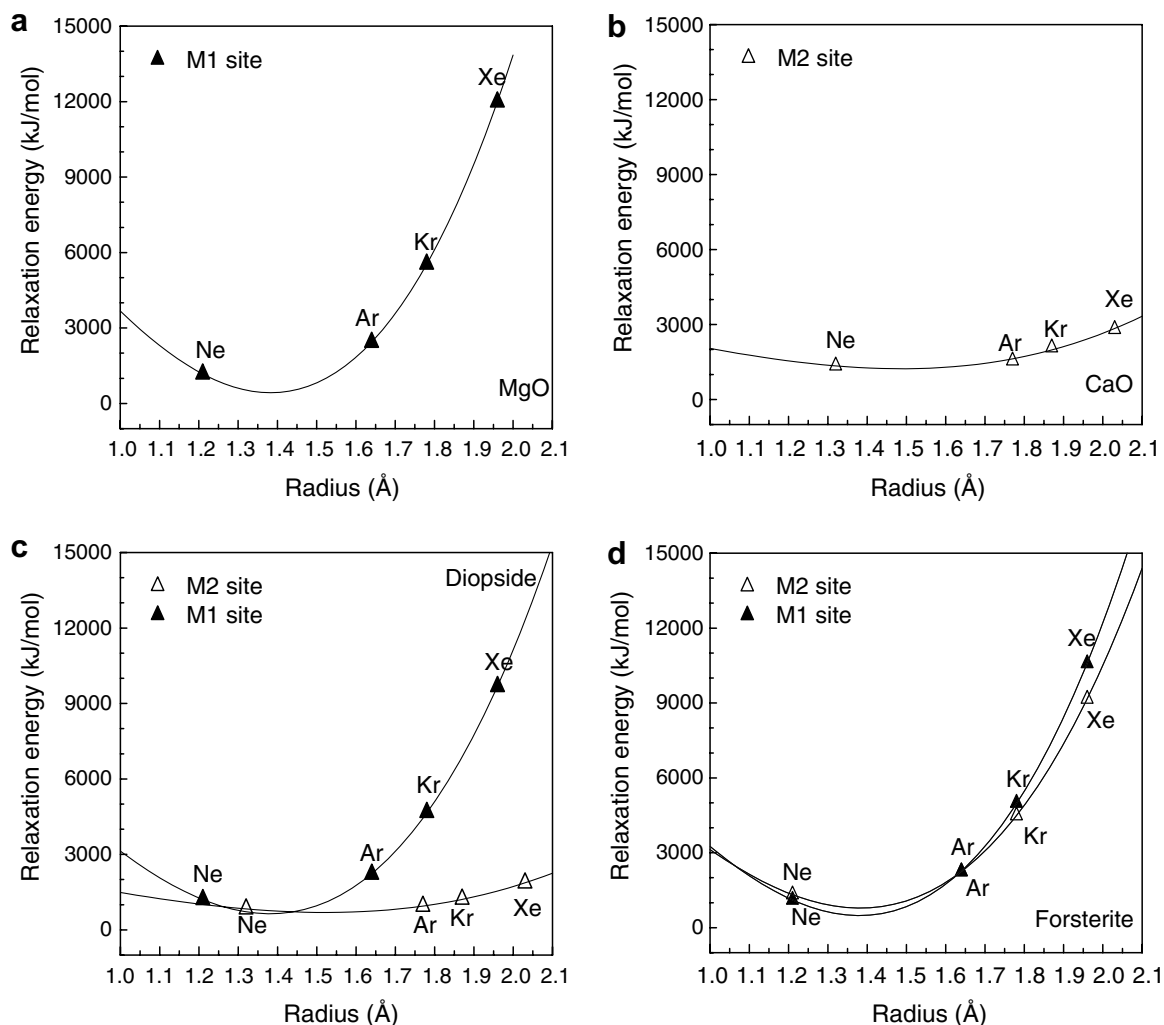


Fig. 3. Variation of relaxation energies for noble gas substitution in (a) MgO, (b) CaO, (c) diopside and (d) forsterite with atomic radius.

Table 3

Apparent site Young's modulus  $E_x$  and the optimum radii of the site  $r_o$  obtained by fitting relaxation energy data (Table 2) to the Brice equation (Eq. (2))

Minerals	Site	$E_x$ (GPa)	$r_o$ (Å)
MgO	Mg	5194	1.38
CaO	Ca	779	1.48
Diopside	Mg(M1)	4026	1.38
	Ca(M2)	651	1.52
Forsterite	Mg(M1)	4494	1.38
	Mg(M2)	3753	1.38

energy, not only includes defect energies but also the differences between the lattice energies of the host and the trace element oxide. What will happen if the local cation environment of the melt is different from that of the binary oxide? To investigate this possibility, we have also calculated the lattice energies of MgO and CaO assuming they have a four- or eight-coordinate structure rather than the sixfold one they actually adopt in the solid-state. The results indi-

cate that in the four-coordination environment the overall solution energies are very similar to those for six-coordination. However, with eight-coordination, the solution energies are much higher. But, in every case, the trends are the same and the curvature of the solution energy vs. atomic radius plot remains unchanged.

Calculated lowest solution energies of noble gas incorporation in MgO, CaO, diopside and forsterite (via the substitution mechanism) are plotted against atomic radius in Fig. 4. The curves are the results of fitting the calculated solution energies to the Brice equation (Eq. (2)). The solution energies, like the relaxation energies, show a near-parabolic dependence on radius. The minimum in solution energies vs. atomic radius occurs at a radius larger than that of the host atom, which is similar to the relaxation energy vs. radius curve (Fig. 3). For all the noble gases the solution energies are positive and the solution energy of Xe is the highest. Fig. 4(c) shows similar features to those in Fig. 2(c), in that the solution energies of noble gas substitution at the M2 site (Ca) in diopside are lower than those at the M1 site (Mg). This indicates that overall the Ca is more favourable than the Mg site for noble gas substitution in

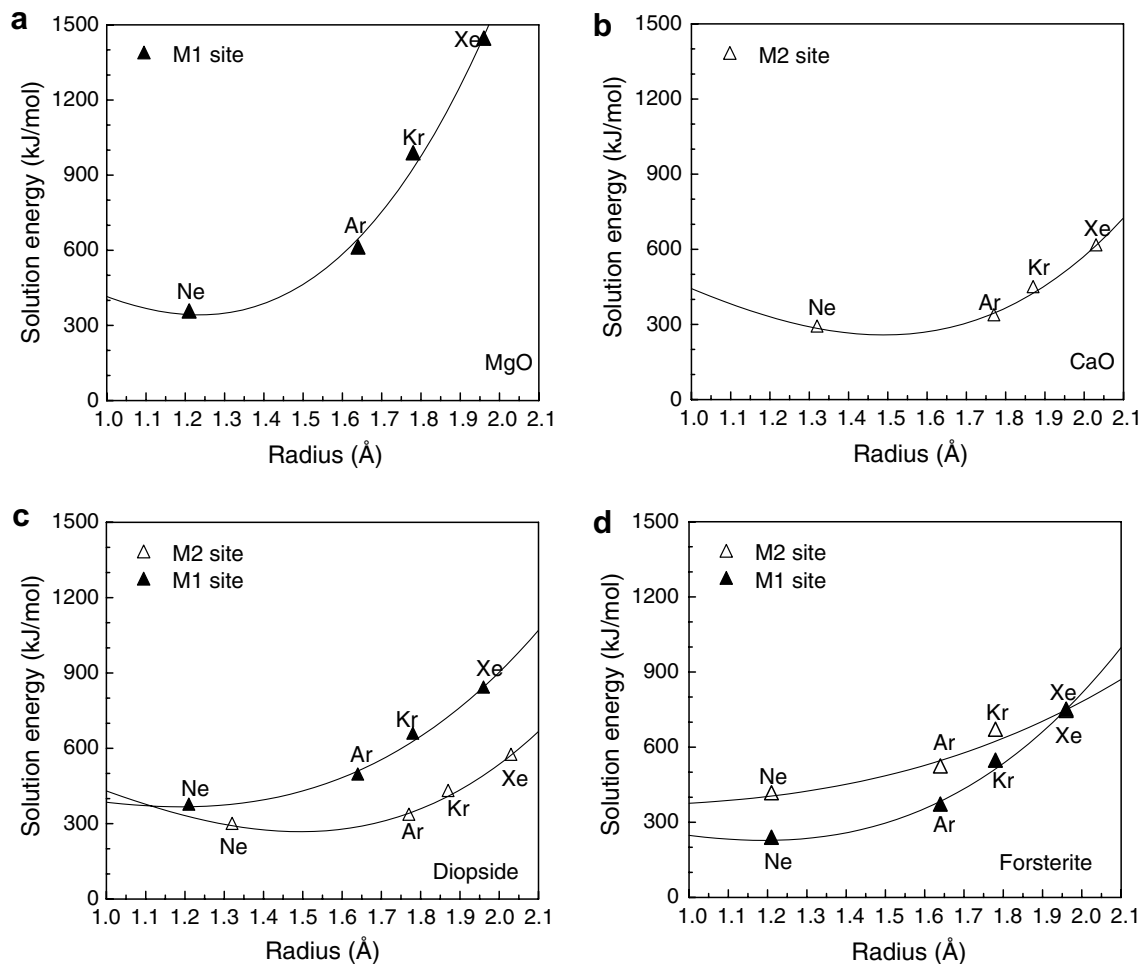
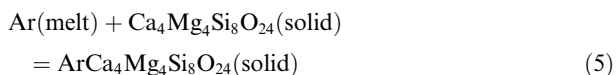


Fig. 4. Variation of solution energies for noble gas substitution in (a) MgO, (b) CaO, (c) diopside and (d) forsterite with atomic radius.

diopside. Additional calculations showed that solution energies with two other 3+ cations (e.g.,  $\text{Al}^{3+}$  or  $\text{Ho}^{3+}$ ) or one 4+ cation (e.g.,  $\text{Zr}^{4+}$  or  $\text{Ti}^{4+}$ ) as compensating defects are larger than those plotted in Fig. 4 but the trends with noble gas radius and variation from one site to another (in the same crystal or from one crystal to another) remain the same, see Fig. 5 for the comparison.

### 3.1.3. Solution energies of noble gas incorporation via an interstitial mechanism

We have also studied incorporation of noble gases via an interstitial mechanism. In this case, there is no need for compensating defects due to the charge of the noble gas, or to assume ideal cation behaviour in the melt. The defect energies are equivalent to the solution energies. An example of such a process (here arbitrarily involving the incorporation of one Ar in a supercell containing four formula units of diopside)



and the energy associated with this process is given by

$$E_{\text{sol}} = E_{\text{def}} \quad (6)$$

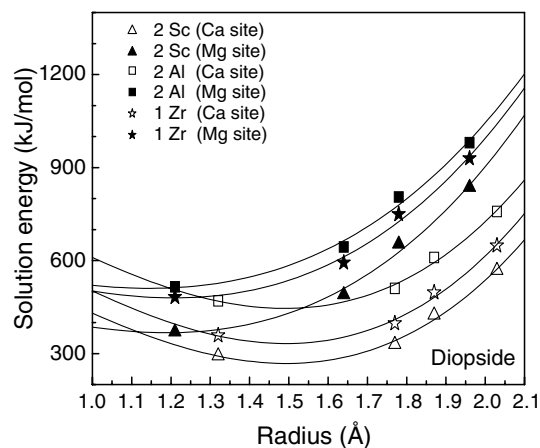


Fig. 5. Variation of solution energies for noble gas substitution at the M1 (Mg) and M2 (Ca) sites in diopside, with different charge-compensation defect(s) including: two  $\text{Sc}^{3+}$  ions, two  $\text{Al}^{3+}$  ions, one  $\text{Zr}^{4+}$  at adjacent cation M1 site(s).

To obtain the lowest solution energies, many different interstitial positions were investigated. Those with the lowest solution energies together with the lowest energies for

incorporation by substitution are listed in Table 4. The initial positions are presented in Appendix B. The order of the solution energy of noble gas interstitial incorporation in all minerals studied is  $\text{Ne} < \text{Ar} < \text{Kr} < \text{Xe}$ . Once again, Xe has the highest solution energy as for substitution incorporation. The results also suggest that there is a connection between the density of the minerals and the favoured mechanism. For the densest mineral, MgO ( $\rho = 3.6182 \text{ g/cm}^3$ ), the solution energies of all noble gas substitutions are always lower than for interstitial incorporation. For forsterite, which has the lowest density of the four minerals studied ( $\rho = 3.1889 \text{ g/cm}^3$ ), the opposite holds and the solution energies of noble gas incorporation via the interstitial mechanism are always lower than those for substitution. The interstitial site is now more favourable. The densities of both CaO ( $\rho = 3.3533 \text{ g/cm}^3$ ) and diopside ( $\rho = 3.2163 \text{ g/cm}^3$ ) are smaller than that of MgO but larger than forsterite. In both CaO and diopside the solution energies of Ar, Kr and Xe substitution are lower than that of interstitial incorporation, while for Ne the interstitial mechanism has lower solution energy, by at least 160 kJ/mol. Hence there is a possibility that Ne is incorporated interstitially in both CaO and diopside. Calculated solution energies of both noble gas substitution and interstitial incorporation in diopside are plotted in Fig. 6. It is clear that for noble gas incorporation in diopside the larger atoms (e.g., Xe, Kr and Ar) prefer crystal sites while smaller atoms, like Ne, tend to occupy interstitial positions.

Table 4

Comparison of solution energies (kJ/mol) for two incorporation mechanisms: lattice site substitution and interstitial

Noble gas	Substitution (Mg site)	Interstitial
<i>MgO</i>		
Ne	348	402
Ar	603	1024
Kr	980	1542
Xe	1437	2005
	Substitution (Ca site)	Interstitial
<i>CaO</i>		
Ne	285	122
Ar	330	454
Kr	442	785
Xe	609	1104
	Substitution (Ca-M2)	Interstitial
<i>Diopside</i>		
Ne	293	123
Ar	329	389
Kr	424	515
Xe	568	773
	Substitution (Mg-M1)	Interstitial
<i>Forsterite</i>		
Ne	230	56
Ar	363	247
Kr	538	444
Xe	742	657

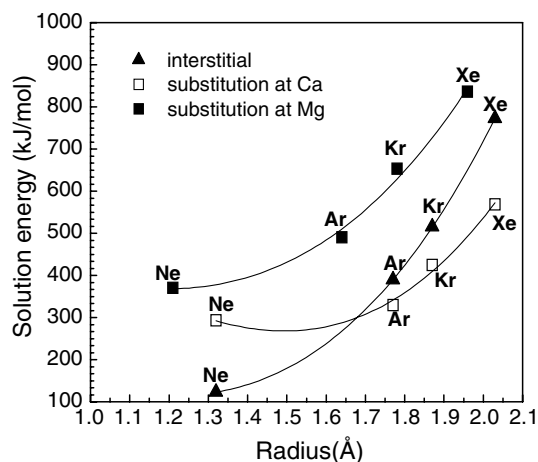


Fig. 6. Calculated solution energies of noble gas incorporation in diopside with (i) noble gas substituted at Ca or Mg site with two  $\text{Sc}^{3+}$  ions as charge-compensation, (ii) noble gas at an interstitial position.

### 3.1.4. Noble gas vs. cation substitution

Fig. 7 compares the calculated solution energies of noble gas substitution in diopside with those of a wide range of trace element cations with different charges, including  $1^+$  ( $\text{Li}^+$ ,  $\text{Na}^+$ ,  $\text{K}^+$  and  $\text{Rb}^+$ ),  $2^+$  ( $\text{Ni}^{2+}$ ,  $\text{Co}^{2+}$ ,  $\text{Fe}^{2+}$ ,  $\text{Mn}^{2+}$ ,  $\text{Cd}^{2+}$ ,  $\text{Eu}^{2+}$ ,  $\text{Sr}^{2+}$  and  $\text{Ba}^{2+}$ ),  $3^+$  ( $\text{Sc}^{3+}$ ,  $\text{Lu}^{3+}$ ,  $\text{Yb}^{3+}$ ,  $\text{Ho}^{3+}$ ,  $\text{Eu}^{3+}$ ,  $\text{Gd}^{3+}$ ,  $\text{Nd}^{3+}$  and  $\text{La}^{3+}$ ) and  $4^+$  ( $\text{Zr}^{4+}$ ,  $\text{Ce}^{4+}$ ,  $\text{U}^{4+}$  and  $\text{Th}^{4+}$ ) ions. For each cation trace element series (except  $2+$  isovalent substitution), associated defects are considered and only the lowest solution energy at the M2 site (Ca) is plotted. For univalent cations incorporated in diopside the lowest mode of solution is  $\text{X}^+(\text{M}2)/\text{Lu}^{3+}(\text{M}1)$ ; for  $3+$  cations it is  $\text{X}^{3+}(\text{M}2)/\text{Na}^+(\text{M}2)$  and for noble gases and

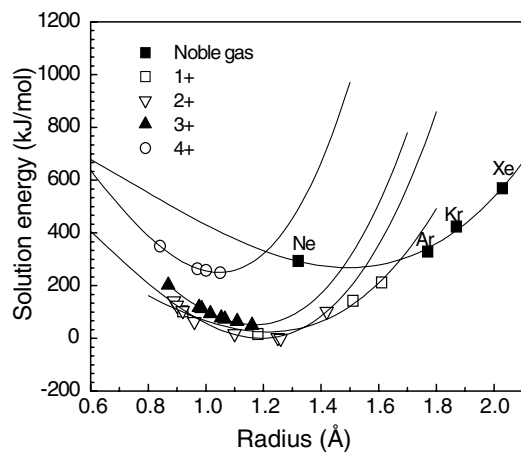


Fig. 7. Variation of calculated solution energy with atomic radius for noble gases and for a range of trace element cations with different charges incorporation in diopside. The cations involved in this study are:  $1^+$  cations: Li, Na, K and Rb,  $2^+$  cations: Mg, Co, Fe, Mn, Cd, Eu, Sr and Ba,  $3^+$  cations are: La, Nd, Eu, Gd, Ho, Yb, Lu and Sc,  $4^+$  cations are: Zr, Ce, U and Th. Each list is in order of increasing ionic radius. Eightfold coordinate radii used for all cations (Shannon, 1976).

4+ cations the lowest modes of solution are  $X^0(M2)/2Sc^{3+}(M1)$  and  $X^{4+}(M2)/2Na^+(M2)$ , respectively. For 2+ cations no charge-compensating defects are required. Fig. 7 shows that the variation of solution energies of all impurities with ionic radius is similar and appears to be roughly parabolic. Once more we have fitted the simulated solution energies to the Brice model (see the curves in Fig. 7). Both parameters  $E_z$ , and  $r_o$  have been extracted from the fitting and are listed in Table 5. The results show that the order of the curvature of these parabola (the effective site modulus,  $E_z$ ) is noble gas <1+ ion <2+ ion <3+ ion <4+ ion. The noble gases thus fall on a more open parabola with less discrimination of the solution energies between one element and another of different size. The optimum radius of the site,  $r_o$ , decreases with increasing charge.

### 3.1.5. Calculation vs. experiment

In Fig. 8, we have displayed the experimentally determined partition coefficients as a function of atomic radius. The data are selected from experiments for trace elements, including noble gases, in diopside-rich clinopyroxene–melt systems (Brooker et al., 2003; Heber et al., 2007). The experiments were carried out at 0.1 GPa and 1200 °C and analysed using a combination of standard ion-probe tech-

Table 5

Extracted apparent site Young's modulus  $E_z$  and the optimum radius  $r_o$  of the site (M2 site) obtained by fitting calculated solution energy data in diopside to the Brice equation (Eq. (2)) for trace elements with different charges

Impurity	$E_z$ (GPa)	$r_o$ (Å)
Noble gas	151	1.49
1+ ion	224	1.21
2+ ion	384	1.19
3+ ion	451	1.17
4+ ion	685	1.04

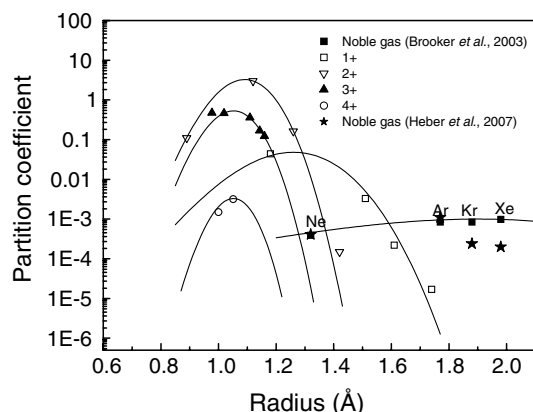


Fig. 8. Experimentally determined mineral–melt partition coefficients for 1+ cations, 2+ cations, 3+ cations, 4+ cations and noble gases from Brooker et al. (2003) and recent data for noble gases from Heber et al. (2007). The 1+ cations are Na, K, Rb and Cs; the 2+ cations are Mg, Ca, Sr and Ba; the 3+ cations are Lu, Nd, Y, Ce, La; the 4+ cations are U and Th. Eightfold coordinate radii (Shannon, 1976) used for all cations.

niques (cations) and ultraviolet laser ablation microprobe (UVLAMP) technique (noble gases). The experimentally determined partition coefficients show very similar features to the calculated solution energies discussed in Section 3.1.4 and shown in Fig. 7. The variation of partition coefficients of all impurities with atomic radius is roughly parabolic and the curvature of the parabola decreases with decreasing cation charge. There are some differences in the magnitude of the curvature, i.e., the “openness” of the parabola between experiments and simulations. This could be due to some simplifying assumptions made in the simulations, such as melt environment or calculation of all energies in the static limit rather than the elevated temperatures of the experiments. Both simulated and experimental data suggest that the solution energies (or partition coefficients) for noble gases are approximately the same as for the 4+ cations (U and Th) as predicted by Wood and Blundy (2001). The results also suggest there will be little fractionation between the heavier noble gases during crystallisation of clinopyroxene from the melt. The extent of agreement between simulation and experiment is very encouraging.

According to the Blundy and Wood (1994) adaptation of the Brice equation, the partition coefficient,  $D_i$ , for an ion with charge  $n+$  and radius  $r_i$  entering a crystal lattice site M can be described in terms of three parameters:  $r_{o(M)}^{n+}$ , the ideal radius of that site for cations with this charge;  $E_z$ , the apparent (effective) Young's Modulus of the site and  $D_{o(M)}^{n+}$  the “strain-free” partition coefficient for a ion with radius  $r_{o(M)}^{n+}$ , the final expression is

$$D_i = D_{o(M)}^{n+} \exp \left\{ -4\pi E_z \left[ \frac{1}{2} r_{o(M)}^{n+} (r_i - r_{o(M)}^{n+})^2 + \frac{1}{3} (r_i - r_{o(M)}^{n+})^3 \right] / k_B T \right\} \quad (7)$$

$D_{o(M)}^{n+}$  and  $E_z$  vary with charge as well as pressure, temperature and melt composition. We now consider the simulated and experimental data in terms of the Brice and the lattice strain model. Fig. 9 plots values of  $E_z$  vs. the ratio of the trace element charge ( $Z$ ) to the “site volume”, taken to equal  $d^3$ , where  $d = r_o + r_o^{2-}$ ,  $r_o$  is the optimum site radius and  $r_o^{2-}$  the ionic radius of  $O^{2-}$ . A value of 1.38 Å is

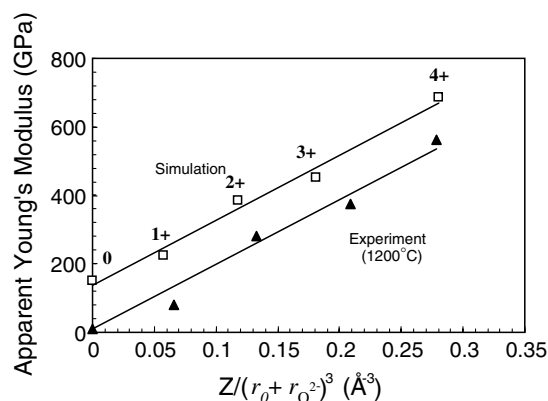


Fig. 9. Apparent site Young's modulus,  $E_z$  vs.  $Z/(r_o + r_o^{2-})^3$  for trace elements of different charge.

assigned to  $r_0^{2-}$  (Shannon, 1976). Two lines are plotted; one corresponding to values of  $E_x$  extracted from experimental partition coefficients and the other to values from simulated solution energies. The existence of these lines and the decrease of the optimum radius with cation charge evident in the plots for both experiment and simulation in Fig. 10, suggest that, in terms of their partitioning behaviour, noble gases behave quite simply as “zero charge cations” (Brooker et al., 2003).

Since the calculations in this paper were completed new melt–mineral experimental partitioning data for forsterite and clinopyroxene have been generated by Heber et al. (2007), which were also presented in Fig. 8. The data for forsterite suggest relatively little fractionation during crystallisation from the melt and the values of the forsterite–melt partition coefficients are similar to those for diopside-rich clinopyroxene–melt systems, both entirely consistent with our calculations. On the basis of experiments in which varying amounts of Sc or Ti were added to the starting materials, Heber et al. (2007) conclude that incorporation of all the noble gases in forsterite is as interstitials. This is consistent with our conclusions in Section 3.1.3 above. However, we should emphasise that even tiny amounts of trace impurities are sufficient to charge-balance noble gas incorporation via a coupled substitution mechanism, such as the replacement of  $3\text{Mg}^{2+}$  by Ar and  $2\text{Sc}^{3+}$  (Eq. (3)), in which the noble gas and its charge-compensating defects are strongly associated. For example, according to Heber et al. (2007), the total solubility of noble gases He–Xe in olivine at 0.1 GPa amounts to just  $1.1 \times 10^{-8} \pm 7 \times 10^{-9}$  mol/g. To charge balance this entire noble gas inventory using  $\text{Sc}^{3+}$  alone requires just  $0.9 \pm 0.6$  ppm (by mass), or in the case of  $\text{Ti}^{4+}$ ,  $0.5 \pm 0.3$  ppm (by mass). We rather doubt that such low contents (i.e.,  $\geq 99.9999\%$  purity) of Sc, Ti or other potential charge-balancing cations, can be eliminated even when using highest grade commercially available reagents. Thus, while we agree with the interpretation of Heber et al. (2007) regarding the likely substitution mechanism of noble gases, we do not consider the experimental modus operandi by which they arrive at this conclusion to be definitive. Similarly, we take issue with the statement of Heber et al. (2007) that,

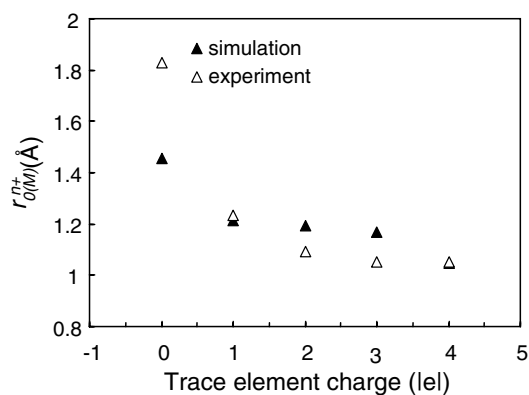


Fig. 10. Optimum site radius,  $r_{o(M)}^{n+}$  as a function of the charge of trace element species.

by analogy with olivines, “[noble gas] partitioning is into sites which are vacant in all clinopyroxenes”, i.e., that all noble gases take up interstitial positions whatever the mineral and whatever the conditions. Our results in Section 3.1.3 show clearly this is not so, with the calculated solution energies indicating that in diopside the larger atoms (e.g., Xe, Kr and Ar) prefer crystal lattice sites while smaller atoms, like Ne, tend to occupy interstitial positions. We conclude that when dealing with trace elements that are highly insoluble in silicate minerals and are incorporated via strongly associated compensating defects, it is very difficult to establish unequivocally by variable level doping alone the favoured substitution mechanism.

### 3.2. Influence of pressure on noble gas incorporation in minerals

In previous sections, we have discussed the defect energies and solution energies of noble gas incorporation (both substitution and interstitial) in CaO, MgO, diopside and forsterite at one atmosphere. In this section, we consider briefly the effects of pressure on the noble gas substitution incorporation. We use the “supercell” method (Taylor et al., 1997) described in earlier section to evaluate directly the defect enthalpies at high  $P$  in the same set of minerals examined.

As before, the noble gas is placed at a Ca or Mg site with two  $\text{Sc}^{3+}$  situated at Mg or Ca sites adjacent to the noble gas (we assume that pressure has no effect on the favoured substitution mechanism). For diopside, only those noble gases substituted at M2 sites are considered. For forsterite, we consider the M1 site only. The solution enthalpy of noble gas incorporation at the diopside Ca site is given by

$$H_{\text{sol}} = H_{\text{df}} - H_{\text{pf}} + H_{\text{lat}}(\text{CaO}) + 2H_{\text{lat}}(\text{MgO}) - H_{\text{lat}}(\text{Sc}_2\text{O}_3) \quad (8)$$

where  $H_{\text{sol}}$  is the solution enthalpy and  $H_{\text{df}}$ ,  $H_{\text{pf}}$  are the enthalpies of the defective and perfect supercells at the pressure of interest.  $H_{\text{lat}}(\text{CaO})$ ,  $H_{\text{lat}}(\text{MgO})$  and  $H_{\text{lat}}(\text{Sc}_2\text{O}_3)$  are the lattice enthalpies of CaO, MgO and  $\text{Sc}_2\text{O}_3$  at the pressure of interest, respectively. The corresponding equation for substitution for  $\text{Mg}^{2+}$  follows immediately. To evaluate the solution enthalpies at high pressure, we have calculated the required lattice energies for CaO, MgO,  $\text{Sc}_2\text{O}_3$  at a range of pressures and these are listed in Table 6. The GULP program was used, as before, for all perfect and defective supercell structure optimisation at high pressure.

For perfect and defective lattice calculations, we first investigate the effect of “supercell” size on the calculated defect energies at one atmosphere pressure to check

Table 6  
Lattice energies (kJ/mol) of binary oxides used to calculate the solution enthalpies at various pressures

Pressure	MgO	CaO	$\text{Sc}_2\text{O}_3$
0.1 MPa	−3986	−3468	−14016
10 GPa	−3877	−3307	−13674
40 GPa	−3570	−2869	−12715

convergence to the dilute limit and determine the most suitable size of the “supercell”. Xe was chosen for these calculations; its large size gives rise to the largest elastic relaxations. The convergence of defect energies with size of the “supercell” is shown in Fig. 11. It is clear that the energies converge to the point-defect limit as the size of “supercell” increases. This suggests an optimum “supercell” size, minimising the computational effort, but without sacrificing accuracy, of 512 atoms for MgO and CaO, 360 atoms for diopside and 336 atoms for forsterite. We have also compared the results of the “supercell” calculations using these cells at one atmosphere with those from the two-region method used earlier and results are plotted in Fig. 12. The good agreement between the two methods leads support to our further use of the “supercell” method to obtain defect and solution enthalpies at high pressure.

The “supercell” method was then used to perform calculations for noble gas substitution in CaO, MgO, diopside and forsterite at  $P = 10$  and 40 GPa. The results indicate that, as expected, solution enthalpies increase with pressure, as shown in Fig. 13. The variation of solution enthalpies of noble gas substitution with the atomic radius is roughly parabolic no matter what type of mineral or what pressure. In all cases, except forsterite, the largest increase in solution

enthalpy with pressure is for Xe. For forsterite the change in solution enthalpy with pressure does not vary significantly from one noble gas to another. We have fitted the simulated solution energies to the Brice model (Eq. (2)), shown as the curves in Fig. 13. Both parameters  $E_x$ , and  $r_o$  are listed in Table 7. The data show that, as expected, apparent site modulus increases with pressure for noble gas incorporated in MgO, CaO and diopside, but no such clear trend is observed in forsterite. The optimum radius of the site decreases with the pressure for all except for MgO at 40 GPa, a particular case which may be an artefact due to the difficulties of fitting to such few points.

### 3.3. Surface vs. bulk incorporation

Surfaces and grain boundaries, whether internal or external, provide a different electrostatic and elastic environment from that of the bulk crystal. Consequently, defect and solution energies may differ substantially at surfaces and grain boundaries from that in the bulk. If surface solution energies are substantially lower than bulk solution energies significant migration of species to the mineral surface will result, and vice versa. It is therefore worthwhile to carry out further simulations and explicitly compare

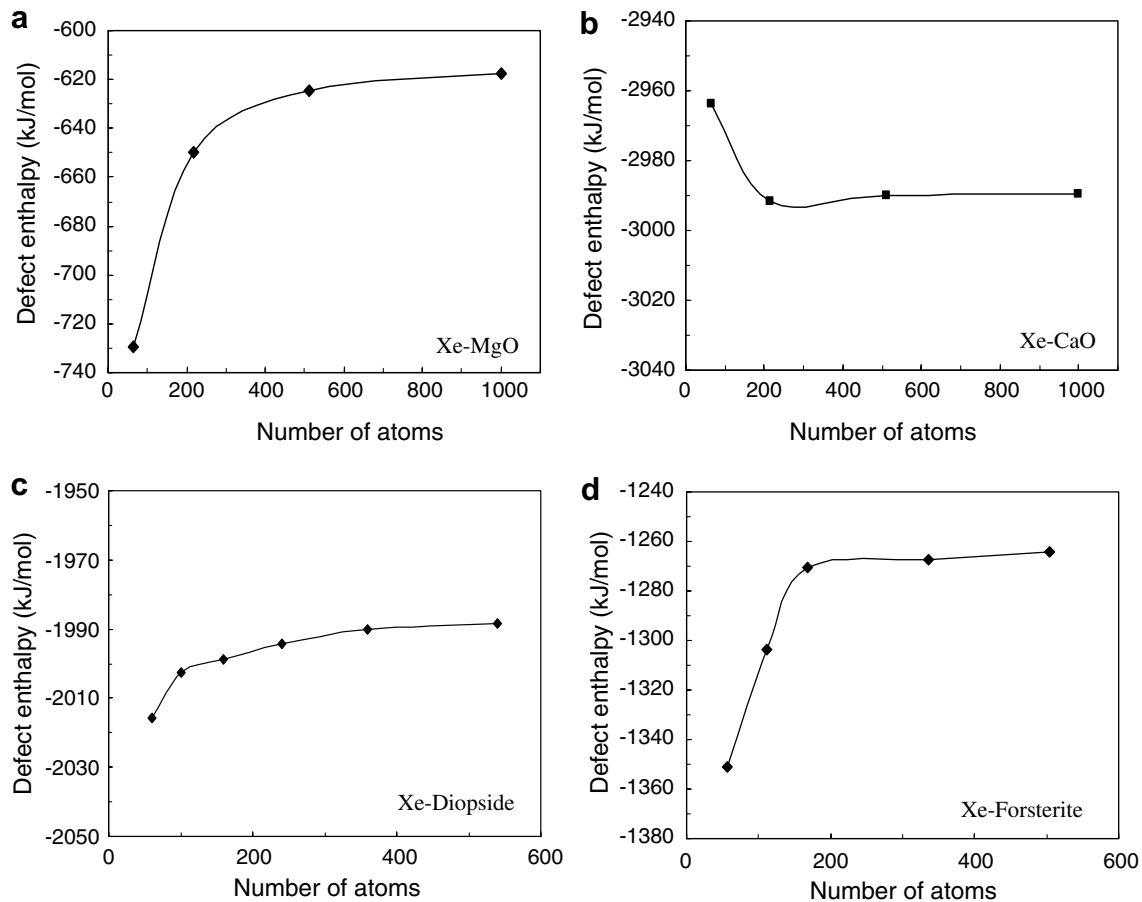


Fig. 11. Variation of calculated defect enthalpies with unit cell size at zero pressure for noble gas substitution incorporation in (a) MgO, (b) CaO, (c) diopside and (d) forsterite.

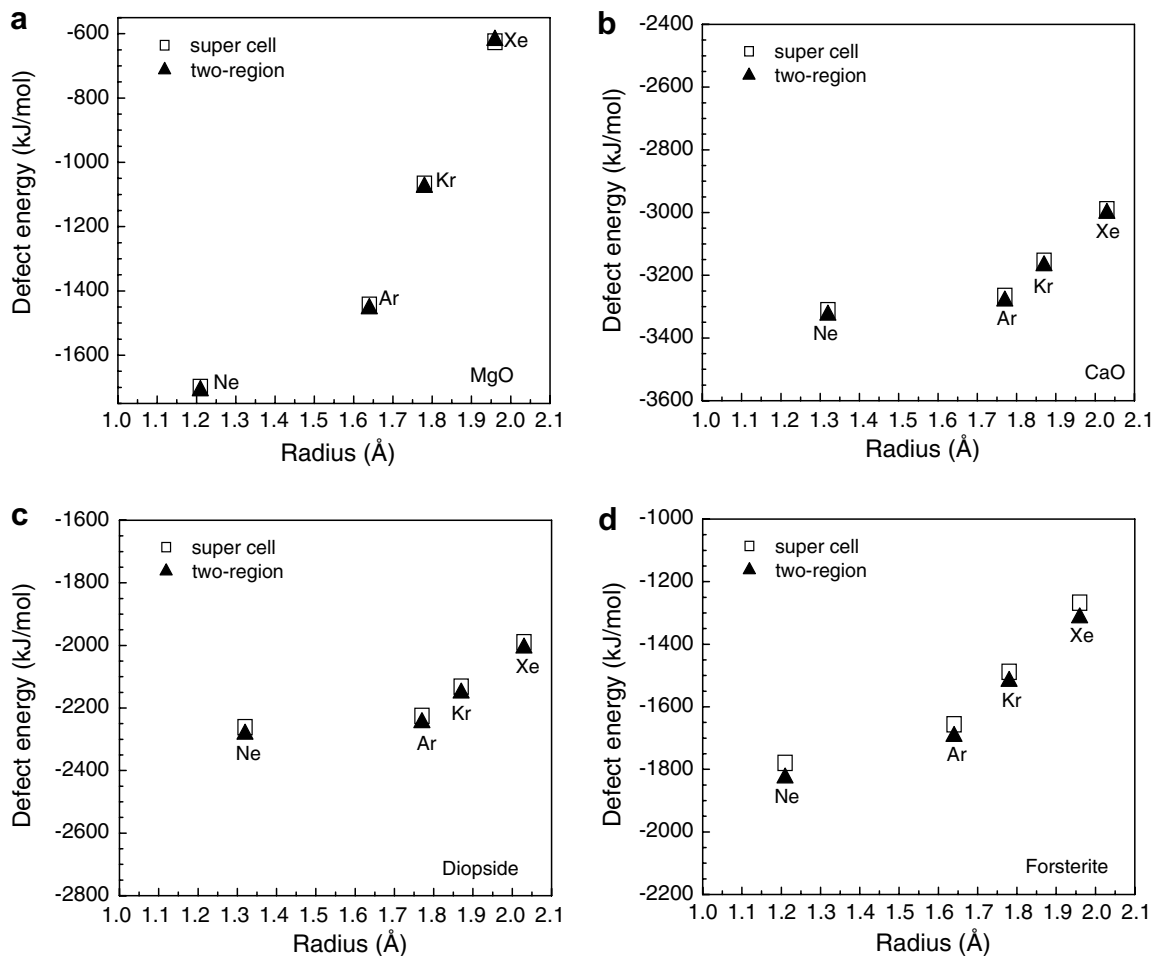


Fig. 12. Comparison of defect energies calculated at atmosphere pressure (0.1 MPa) using the supercell method and the two-region approach for noble gas incorporated in (a) MgO, (b) CaO, (c) diopside and (d).

calculated solution energies in the bulk with those at the surface. We have used MgO as a representative mineral. A slab of MgO, terminated at top and bottom by the (001) surface, with surface area  $\sim 282 \text{ \AA}^2$  (512 atoms), is separated by a vacuum gap from its periodic images. To test convergence, calculations were conducted for a series of slab thickness and gap widths which indicated that a slab thickness of eight layers ( $\approx 17 \text{ \AA}$ ) and a gap width of about  $25 \text{ \AA}$  were sufficient for the calculations reported here. Surface defect energies are calculated by a supercell method. Initially, the geometry of the undefective (perfect) slab is optimized at constant volume, i.e., cell with fixed dimensions. The noble gases and the compensating defects are then introduced at the surface. The noble gas atom is placed at a Mg surface site and two Sc atoms replace two Mg atoms at the surface Mg sites nearest to the noble gas. The geometry of the slab is reoptimized at constant volume. The surface solution energy ( $E_{s-sol}$ ) is

$$E_{s-sol} = E_{d-surf} - E_{p-surf} + 3E_{lat}(\text{MgO}) - E_{lat}(\text{Sc}_2\text{O}_3) \quad (9)$$

where  $E_{d-surf}$ ,  $E_{p-surf}$  are the energies of the defective and perfect (undefective) slabs, respectively. For the bulk, once again the supercell method is used for the defect en-

ergy calculations, where the number of atoms is same as to that used in surface calculations. Both bulk and surface calculated results are listed in Table 8. It is clear from the calculated results that in all cases, the solution energy of a noble gas substituted at a surface site is lower than in the bulk and the solution energy for surface incorporation decreases with the size of the noble gas atom, a trend opposite to that in solution energies observed for bulk incorporation. At the surface, the difference in solution energy between different noble gases is much smaller than that in the bulk. For heavy atoms (e.g., Xe) the energy difference for substitution in the bulk and at surface is very large with the solution energy for surface substitution approximately a seventh that in the bulk. For small atoms the difference is smaller (e.g., about two-thirds for Ne). This indicates that there is pronounced segregation of Xe at the (001) surface.

The solubility of the heavier noble gases may thus be considerably enhanced by the presence of interfaces and other extended defects. This is consistent with the experimental study studies of Brooker et al. (1998), Wartho et al. (1999) and Chamorro et al. (2002), who observed unusually high concentrations of argon at analysed crys-

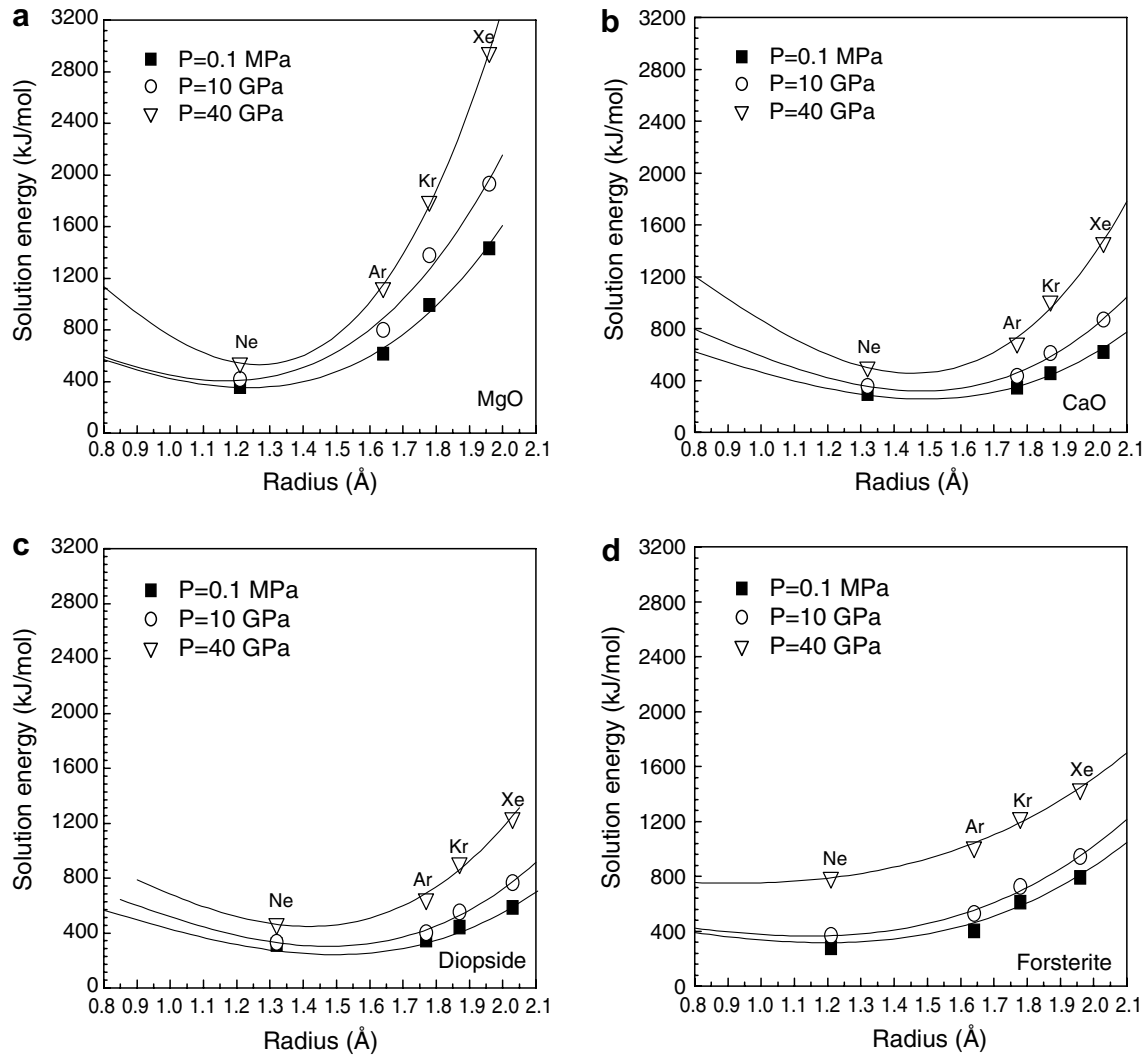


Fig. 13. Calculated solution enthalpies vs. atomic radius (Å) in (a) MgO, (b) CaO, (c) diopside and (d) forsterite at  $P = 0.1$  MPa, 10 and 40 GPa using the “supercell” method.

Table 7

The effect of pressure on apparent site Young’s modulus  $E_z$  and the optimum radius  $r_o$  of the site of noble gas incorporated in MgO, CaO, diopside and forsterite

Materials	Pressure	$E_z$ (GPa)	$r_o$ (Å)
MgO	0.1 MPa	324	1.23
	10 GPa	390	1.17
	40 GPa	771	1.26
CaO	0.1 MPa	194	1.49
	10 GPa	264	1.48
	40 GPa	448	1.45
Diopside	0.1 MPa	172	1.49
	10 GPa	218	1.47
	40 GPa	311	1.41
Forsterite	0.1 MPa	131	1.19
	10 GPa	138	1.14
	40 GPa	103	0.90

Table 8

Solution energies (kJ/mol) of noble gas incorporated in MgO bulk vs. at its surface, calculated via supercell calculations

Noble gas	Bulk	Surface
Ne	358	221
Ar	614	216
Kr	991	213
Xe	1433	208

The small differences between the bulk defect energies here and those in Table 4 arise since the former obtained from supercell calculations while the latter are point-defect energies calculated using the Mott–Littleton technique (see text).

tal surfaces. For the exposed surfaces in diffusion experiments this concentration is far in excess of the amount expected, given the projected diffusion profile observed

at depth in the same analysis pit. For freshly exposed surfaces (i.e., sectioned partitioning experiments) a high surface concentration of heavier noble gas is sometime observed compared to concentrations in deeper analyses that are thought to represent bulk solubility. This may represent redistribution of the gas during/after sectioning as a relaxed lattice surface is created. The fact that the surfaces analysed in the partitioning experiments were cut after the experiment was quenched, may suggest that migration to a surface via diffusion can occur on short timescales and is a serious consideration for any experimentalist wishing to measure heavy noble gas concentrations in sectioned run products. This is in addition to problems with the diffusive loss of the lighter noble gases (He and Ne) from crystal surfaces at room temperature as observed by Heber et al. (2007). Anomalously high ‘hot spots’ of argon concentration, compared with average values were observed on the surface of quartz grains by Roselieb et al. (1997), who argued that some previous experimental studies (e.g., Broadhurst et al., 1990, 1992) showing unusually high noble gas partition coefficients were a consequence of surface enrichment of the noble gas.

#### 4. CONCLUSIONS

In this study, we have used the Grand Canonical Monte-Carlo technique to determine potential parameters between noble gas and silicate minerals by fitting to available adsorption isotherm data. The resulting parameters were then used to study possible mechanisms of noble gas incorporation in minerals.

The two-region approach was used to study the mechanisms of noble gas incorporation in a variety of minerals including MgO, CaO, diopside and forsterite. There appears to be a correlation between the density of the materials and the favoured mechanism. For the densest mineral, MgO, a lattice site seems to be more favourable than an interstitial position for all the noble gases studied. For forsterite, which has the lowest density of the four materials studied, the opposite holds and an interstitial position is favoured over a lattice site for all noble gases. Heavy noble gases, such as Ar, Kr and Xe, prefer to enter the Ca lattice site in diopside and CaO rather than an interstitial position. For light noble gases (e.g., Ne) in the same minerals it is possible that the interstitial mechanism dominates.

The variation of solution energies of noble gas substitution in CaO, MgO, diopside and forsterite with their atomic radii is roughly parabolic, analogous to those of  $1^+$ ,  $2^+$ ,  $3^+$  and  $4^+$  trace element cations incorporated in diopside. Our simulated results also indicate that the apparent site Young’s modulus ( $E_s$ ) vs. the ratio of charge to site volume for all trace elements in diopside is a linear relationship and the optimum radius,  $r_o$ , increases with decreasing charge. Both features are consistent with high temperature partitioning experiments (Blundy and Wood, 2003). Our results suggest that noble gases enter crystal lattices in just the same way as cations, causing lattice strain due to the size and charge mis-

match, and are therefore subject to the same thermodynamic controls on crystal–melt partitioning.

At high pressures the variation of solution energy with the atomic radius of noble gas remains nearly parabolic. Solution energies increase with the atomic number of the noble gas and strongly depend on the pressure, especially for the largest noble gases, such as Xe. The behaviour of noble gases in these dense materials is thus very different from that in porous materials such as zeolites and their behaviour is consistent with that expected by extrapolation from that of trace element cations. We also predict pronounced segregation to mineral surfaces and that the solubility of the heavier noble gases may be enhanced considerably by the presence of extended defects such as interfaces. In future work it will be of particular interest to extend our studies to consider noble gas diffusion as well as the thermodynamics of incorporation.

#### ACKNOWLEDGMENT

This work was supported by NERC Grant GR3/A9772. JDB acknowledges a Senior Research Fellowship from NERC.

#### APPENDIX A

The derivation of the potentials involving the noble gases and solid.

Lennard-Jones potentials are used for the gas–solid and gas–gas interactions:

$$U(r_{ij}) = \begin{cases} 4\varepsilon_{ij} \left[ \left( \frac{\sigma_{ij}}{r_{ij}} \right)^{12} - \left( \frac{\sigma_{ij}}{r_{ij}} \right)^6 \right] & r_{ij} \leq r_c \\ 0 & r_{ij} > r_c \end{cases} \quad (10)$$

where  $r_c$  is the cut-off distance. A major task here is the determination of the gas–solid interaction parameters,  $\varepsilon_{ij}$  and  $\sigma_{ij}$ . These were first obtained for the interaction of argon with atoms of the solid by fitting to experimental adsorption isotherms for Ar in a range of zeolites, as described in more detail below. Adsorption isotherms are calculated using the Grand Canonical Monte-Carlo (GCMC) technique (Frenkel and Smit, 2002). The Monte-Carlo simulations are carried out within the  $\mu VT$  ensemble. During the simulation chemical potential, temperature and box volume ( $\mu, T, V$ ) are kept constant and the number of molecules in the box is allowed to fluctuate. Many previous Monte-Carlo simulations in zeolites have usually assumed a rigid framework for the zeolites (Mooij et al., 1992; Smit and Siepmann, 1994; Vlugt et al., 1999). In our GCMC simulations, all zeolite frameworks are flexible. There are three types of trial movements involved in GCMC simulations. In addition to particle displacements that include atoms both in the gas and the crystal, attempts at adding or removing a gas particle to or from the simulation box are also made. At each simulation step, one of the movements described above is randomly selected. In the course of displacement, one particle (either a gas or a solid atom) is randomly chosen and then given a randomly selected

displacement. During the simulation the maximum displacement is adjusted to achieve an overall acceptance of 50%. According to the energy of the new configuration, the movement is accepted or rejected using the Metropolis algorithm (Metropolis et al., 1953). If the movement is accepted then the system will be updated. Otherwise, it will stay in the old configuration. For displacement of a particle this takes the form

$$\text{acc}(o \rightarrow n) = \min \left[ 1, \exp \left\{ -\frac{1}{k_B T} [U(n) - U(o)] \right\} \right] \quad (11)$$

where  $\text{acc}(o \rightarrow n)$  is the acceptance probability of a move from an old configuration to a new configuration.  $U(n)$  and  $U(o)$  are the potential energies of the new and old configurations, respectively.  $k_B$  is Boltzmann's constant.

For the insertion/removal of a gas particle, it is randomly decided whether an attempt is made to insert or to remove a randomly selected particle. For particle insertion:

$$\begin{aligned} \text{acc}(o \rightarrow n) \\ = \min \left[ 1, \frac{V}{\Lambda^3(N+1)} \exp \left\{ \frac{1}{k_B T} [\mu - U(n) + U(o)] \right\} \right] \end{aligned} \quad (12)$$

where  $\Lambda (=h/(2\pi mk_B T)^{1/2})$  is the thermal de Broglie wavelength of the noble gas atom and  $m$  the mass of the noble gas atom.  $N$  is the instantaneous number of particles.  $\mu$  is the chemical potential and  $V$  is the volume of the simulation box. It is assumed that the volume of the reservoir is much larger than the volume of the zeolite cavity and the bulk noble gas phase is treated as an ideal gas.

For particle removal:

$$\begin{aligned} \text{acc}(o \rightarrow n) \\ = \min \left[ 1, \frac{\Lambda^3 N}{V} \exp \left\{ -\frac{1}{k_B T} [\mu + U(n) - U(o)] \right\} \right] \end{aligned} \quad (13)$$

The GCMC technique mimics a zeolite in contact with a reservoir (in this case noble gas). The reservoir keeps the temperature and chemical potential of each component constant, whereas the number of particles is allowed to fluctuate during the simulations. The adsorbed noble gas molecules (inside the zeolite) are in equilibrium with the gas in the reservoir. The equilibrium conditions are such that the temperature and chemical potential of each component of the gas inside and outside the adsorbent must be equal. For each simulation the bulk-gas pressure  $P$  and temperature  $T$  are specified. To generate an adsorption isotherm a wide range of pressures, 0–1000 kPa, is selected for each temperature.

We assume all the interaction parameters are transferable from silicate minerals to zeolites. Firstly, we carried out Monte-Carlo simulations for silicalite, mordenite and 5A zeolites in the static limit at constant pressure (zero) to obtain optimised zeolite structures. Table 9 compares calculated and experimental lattice parameters for the zeolites used for isotherm generation. Lattice parameters are reproduced to within 2.3% of the experimental data. For silicalite zeolite, a simulation box was constructed by

Table 9

Comparison between calculated static limit and experimental (in parentheses) lattice parameter of the three zeolites used to obtain noble gas/mineral potential parameters

Zeolites	Lattice parameters (Å)		
	<i>A</i>	<i>B</i>	<i>C</i>
Silicalite	(20.022) <sup>a</sup>	(19.899)	(13.383)
	20.424	20.298	13.652
Mordenite	(17.920) <sup>b</sup>	(20.310)	(7.480)
	18.338	20.784	7.650
5A	(12.420) <sup>c</sup>	(12.420)	(12.420)
	12.542	12.542	12.542

<sup>a</sup> Van Koningsveld et al. (1987).

<sup>b</sup> Schlenker et al. (1979).

<sup>c</sup> Seff and Shoemaker (1967).

$2 \times 2 \times 2$  replication of the unit cell with side lengths 40.848, 40.596 and 27.304 Å containing 2304 atoms. For 5A zeolite, a cubic lattice with side length 25.084 Å containing eight unit cells and 640 atoms was used as a simulation box. The simulation box for mordenite zeolite has side lengths of 36.676, 41.572 and 30.600 Å consisting of 16 unit cells and 2432 atoms. In the implementation of the Monte-Carlo simulation, the system first was equilibrated for  $10^6$  cycles, after which data were collected for another  $10^6$  cycles.

We use the conventional 'mixing' rules to obtain interatomic potentials. The Lennard-Jones energy parameter for the interaction between atoms  $i$  and  $j$ ,  $\varepsilon_{ij}$ , is given by the geometric mean of the pure atom values,

$$\varepsilon_{ij} = \sqrt{\varepsilon_i \varepsilon_j} \quad (14)$$

and the corresponding Lennard-Jones size parameter  $\sigma_{ij}$  is the arithmetic mean of the pure atom values,

$$\sigma_{ij} = \frac{\sigma_i + \sigma_j}{2} \quad (15)$$

Values of  $\varepsilon_i$  and  $\sigma_i$  for Kr and Xe were taken from Cuadros et al. (1996). For Ne, for which no parameterisation is given by Cuadros et al. (1996), we used values from Hirschfelder et al. (1964). We used the Lennard-Jones size parameters  $\sigma_i$  for the pure atoms in the zeolite and the  $\varepsilon_i$  and  $\sigma_i$  values for pure Ar listed by Watanabe et al. (1995). The required  $\sigma_{ij}$  parameters were calculated from this set of  $\sigma_i$ . We then carried out GCMC calculations to derive the Lennard-Jones energy parameters (namely,  $\varepsilon_{ij}$ ) for the argon–oxygen and argon–cation interactions by fitting to experimental adsorption isotherms of argon in these three zeolites. We first guessed an  $\varepsilon_{\text{Ar-O}}$  value and performed a series of simulations of argon adsorption in silicalite zeolite at 298 K over a range of pressures (0–700 KPa) to generate an adsorption isotherm. The simulated isotherm was then compared with the available experimental data (Watanabe et al., 1995). We adjusted the  $\varepsilon_{\text{Ar-O}}$  parameter until the simulated isotherm reproduced the experimental adsorption isotherm well (see Fig. 14(a)). As our first test, we then used the resulting  $\varepsilon_{\text{Ar-O}}$  parameter to determine a further isotherm for argon in the same zeolite

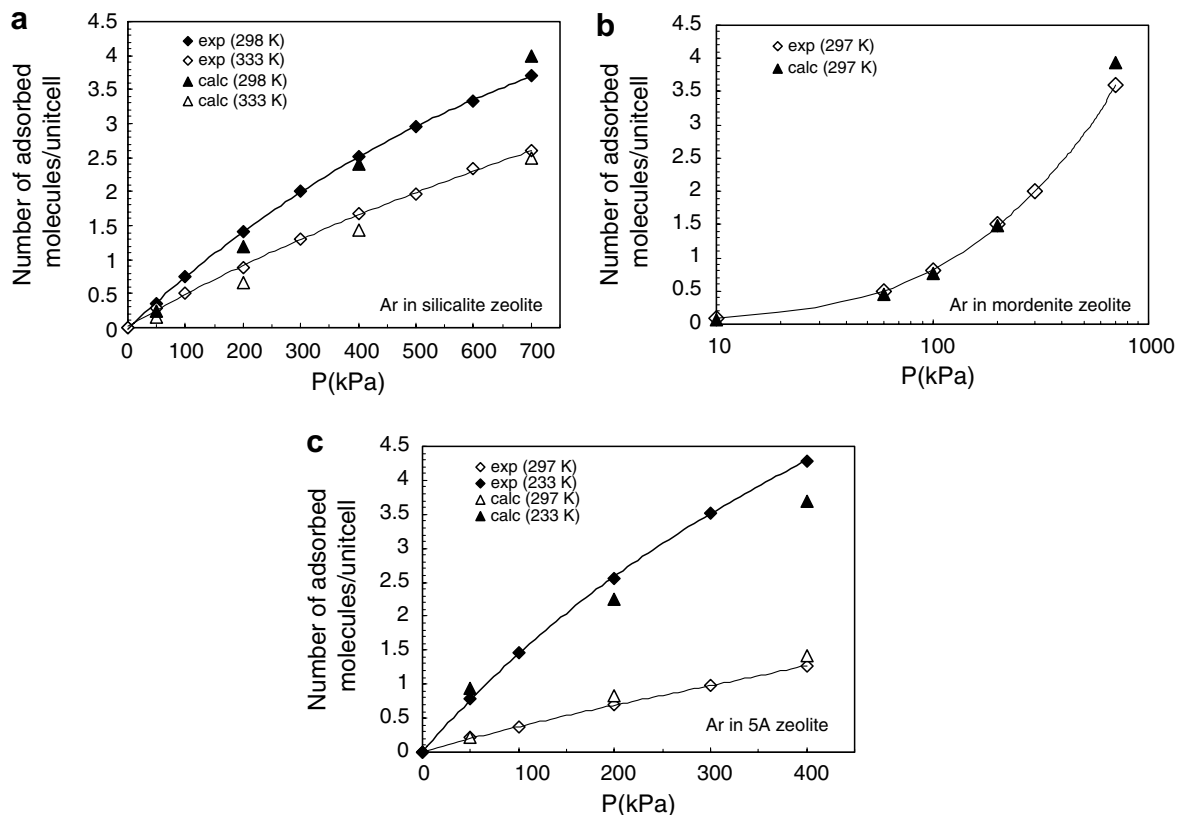


Fig. 14. Simulated adsorption isotherms compared to those from experiment. (a) Adsorption isotherms of Ar in silicalite zeolite at 298 and 333 K (experimental data from Watanabe et al. (1995)), (b) adsorption isotherms of Ar in mordenite zeolite at 297 K (experimental data from Macedonia et al. (2000)), (c) adsorption isotherms of Ar in 5A zeolite at 233 and 297 K (experimental data from Miller et al. (1987)). More details are given in the text.

at 333 K and compared with the corresponding experimental result. As shown in Fig. 14(a) agreement is satisfactory. Next, we carried out simulations of argon adsorption in mordenite zeolite, keeping the  $\epsilon_{\text{Ar-O}}$  parameters derived from silicalite zeolite fixed, but varying  $\epsilon_{\text{Ar-Na}}$  for the Na–Ar interaction. In this case, experimental data of Macedonia et al. (2000) were available for fitting. Finally, adsorption data for the 5A zeolite (Miller et al. (1987)) were used to obtain the  $\epsilon$  parameter for Ar–Ca. Final simulated and experimental isotherms for argon on mordenite and 5A zeolite are shown in Fig. 14(b) and (c). Fig. 14 shows that overall the agreement between the simulation and experiment is good. The calculated isotherms are most sensitive to the Ar–O potential. Based on the  $\epsilon$  parameters of Ar–O, Ar–Si, Ar–Ca and Ar–Na we then calculate the Lennard-Jones  $\epsilon$  parameters between the gas–solid for the other noble gases using Eq. (14).

To test the resulting parameters we have used available experimental data for Xe adsorption (Shen, 1991). The calculated isotherm together with the experimental isotherm is shown in Fig. 15. Agreement is excellent. Unfortunately we have been unable to find further experimental data to refine our parameter set. We assume that all these interaction parameters are transferable from noble gas–zeolites to noble gas–silicate minerals.

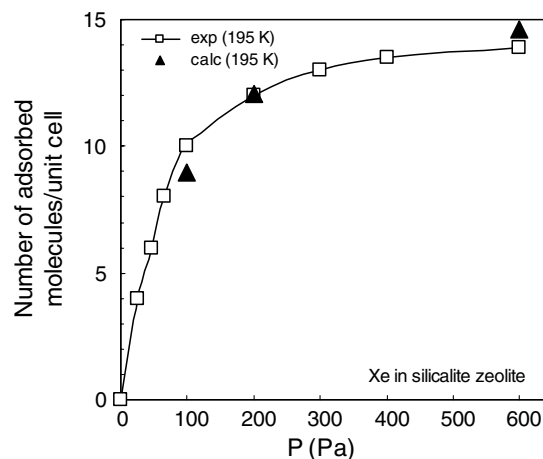


Fig. 15. Simulated and experimental (Shen, 1991) adsorption isotherms of Xe in silicalite zeolite at 195 K.

## APPENDIX B

Initial configurations leading after minimisation to the lowest energies for noble gas interstitial incorporation in CaO, MgO, diopside and forsterite.

CaO					
<i>Lattice parameters</i>					
4.8105	4.8105	4.8105	90.00	90.00	90.00
<i>Fractional coordinates</i>					
Ca	0.0	0.0	0.0		
Ca	0.0	0.5	0.5		
Ca	0.5	0.0	0.5		
Ca	0.5	0.5	0.0		
O	0.5	0.5	0.5		
O	0.5	0.0	0.0		
O	0.0	0.5	0.0		
O	0.0	0.0	0.5		
Xe	0.25	0.25	0.25		

MgO					
<i>Lattice parameters</i>					
4.212	4.212	4.212	90.00	90.00	90.00
<i>Fractional coordinates</i>					
Mg	0.0	0.0	0.0		
Mg	0.0	0.5	0.5		
Mg	0.5	0.0	0.5		
Mg	0.5	0.5	0.0		
O	0.5	0.5	0.5		
O	0.5	0.0	0.0		
O	0.0	0.5	0.0		
O	0.0	0.0	0.5		
Xe	0.25	0.25	0.25		

Diopside					
<i>Lattice parameters</i>					
	13.319262	6.659631	5.241675	78.927780	101.072220
	94.811933				
<i>Fractional coordinates</i>					
Ca	0.1507500	0.3015000	0.2500000		
Ca	0.6507500	0.3015000	0.2500000		
Ca	0.3514573	0.7029147	0.7500000		
Ca	0.8514573	0.7029147	0.7500000		
Mg	0.4535960	0.9071921	0.2500000		
Mg	0.9535960	0.9071921	0.2500000		
Mg	0.0486112	0.0972225	0.7500000		
Mg	0.5486112	0.0972225	0.7500000		
Si	0.1883297	0.8161526	0.2058618		
Si	0.6883297	0.8161526	0.2058618		
Si	0.4080763	0.3766595	0.2941381		
Si	0.9080763	0.3766595	0.2941381		
Si	0.3138775	0.1882620	0.7941381		
Si	0.8138775	0.1882620	0.7941381		
Si	0.0941310	0.6277551	0.7058618		
Si	0.5941310	0.6277551	0.7058618		
O	0.1000397	0.9769917	0.1356449		
O	0.6000397	0.9769917	0.1356449		
O	0.4884958	0.2000795	0.3643550		
O	0.9884958	0.2000795	0.3643550		
O	0.4021676	0.0274229	0.8643550		
O	0.9021676	0.0274229	0.8643550		
O	0.0137114	0.8043352	0.6356449		
O	0.5137114	0.8043352	0.6356449		
O	0.3021767	0.8979879	0.2843020		
O	0.8021767	0.8979879	0.2843020		
O	0.4489939	0.6043535	0.2156979		

Diopside			
O	0.9489939	0.6043535	0.2156979
O	0.2000305	0.1064267	0.7156979
O	0.7000305	0.1064267	0.7156979
O	0.0532133	0.4000611	0.7843020
O	0.5532133	0.4000611	0.7843020
O	0.1807478	0.6645757	0.9810432
O	0.6807478	0.6645757	0.9810432
O	0.3322878	0.3614956	0.5189567
O	0.8322878	0.3614956	0.5189567
O	0.3214595	0.3398389	0.0189567
O	0.8214595	0.3398389	0.0189567
O	0.1699194	0.6429190	0.4810432
O	0.6699194	0.6429190	0.4810432
Xe	0.5000000	0.5000000	0.5000000

Forsterite						
<i>Lattice parameter</i>						
4.776739	10.248095	5.987122	90.000000	90.000000	90.000000	
<i>Fractional coordinates</i>						
Mg	0.0000000	0.0000000	0.0000000			
Mg	0.5000000	0.5000000	0.9999999			
Mg	0.5000000	0.5000000	0.4999999			
Mg	0.9999999	0.0000000	0.4999999			
Mg	0.9979086	0.2830221	0.2499999			
Mg	0.4979086	0.2169778	0.7499999			
Mg	0.5020913	0.7830221	0.2500000			
Mg	0.0020913	0.7169778	0.7500000			
Si	0.4446726	0.0979293	0.2499999			
Si	0.9446726	0.4020706	0.7499999			
Si	0.0553273	0.5979293	0.2499999			
Si	0.5553273	0.9020706	0.7499999			
O	0.7841050	0.0925246	0.2499999			
O	0.2841050	0.4074753	0.7499999			
O	0.7158949	0.5925246	0.2499999			
O	0.2158949	0.9074753	0.7500000			
O	0.2104659	0.4527612	0.2499999			
O	0.7104659	0.0472387	0.7499999			
O	0.2895340	0.9527612	0.2499999			
O	0.7895340	0.5472387	0.7499999			
O	0.2926881	0.1648065	0.0343755			
O	0.7926881	0.3351934	0.9656244			
O	0.2073118	0.6648065	0.4656244			
O	0.7073118	0.8351934	0.5343755			
O	0.7073118	0.8351934	0.9656244			
O	0.2073118	0.6648065	0.0343755			
O	0.7926881	0.3351934	0.5343755			
O	0.2926881	0.1648065	0.4656244			
Xe	0.5233700	0.3317700	0.3841000			

## REFERENCES

- Allan and Cooper, 1987 Allan N. L. and Cooper D. L. (1987) Local density approximations and momentum-space properties in light molecules and ionic solids, *J. Chem. Soc., Faraday Trans. 2* **83**, 1675–1687.
- Allan N. L., Mackrodt W. C. and Leslie M. (1987) Calculated point-defect entropies in MgO. *Adv. Ceram.* **23**, 257–271.
- Allan N. L. and Mackrodt W. C. (1993) Simulation studies of structural and defect properties of high temperature superconducting materials. *Adv. Solid State Chem.* **3**, 221–269.

- Allan N. L., Blundy J. D., Purton J. A., Lavrentiev M. Yu. and Wood B. J. (2001). *EMU Notes in Mineralogy* **3**, 251, Chapter 11.
- Allègre C. J., Staudacher T. and Sarda P. (1987) Rare gas systematics: formation of the atmosphere, evolution and structure of the Earth's mantle. *Earth Planet. Sci. Lett.* **81**, 127–150.
- Allègre C. J., Hofman A. and O'Nions K. (1996) The Argon constraints on mantle structure. *Geophys. Res. Lett.* **23**, 3555–3557.
- Blundy J. D. and Wood B. J. (1994) Prediction of crystal–melt partition coefficients from elastic moduli. *Nature* **372**, 452–454.
- Blundy J. D. and Wood B. J. (2003) Partitioning of trace elements between crystals and melts. *Earth Planet. Sci. Lett.* **210**, 387–397.
- Brice J. C. (1975) Some thermodynamic aspects of the growth of strained crystals. *J. Crystal Growth* **28**, 249–253.
- Broadhurst C. L., Drake M. J., Hagee B. E. and Bernatowicz T. J. (1990) Solubility and partitioning of Ar in anorthite, diopside, forsterite, spinel and synthetic basal liquids. *Geochim. Cosmochim. Acta* **54**, 299–309.
- Broadhurst C. L., Drake M. J., Hagee B. E. and Bernatowicz T. J. (1992) Solubility and partitioning of Ne, Ar, Kr and Xe in minerals and synthetic basaltic melts. *Geochim. Cosmochim. Acta* **56**, 709–723.
- Brooker R. A., Du Z., Blundy J. D., Kelley S. P., Allan N. L., Wood B. J., Chamorro E. M., Wartho J. A. and Purton J. A. (2003) The 'zero' charge partitioning behaviour of noble gases during mantle melting. *Nature* **423**, 738–741.
- Brooker R. A., Wartho J.-A., Carroll M. R., Kelley S. P. and Draper D. S. (1998) Preliminary UVLAMP determinations of argon partition coefficients for olivine and pyroxene grown from silicate melts. *Chem. Geol.* **147**, 185–200.
- Catlow C. R. A., Corish J., Jacobs P. W. M. and Lidiard A. B. (1981) The thermodynamics of characteristic defect parameters. *J. Phys. C: Solid State Phys.* **14**, L121–L125.
- Catlow C. R. A. and Mackrodt W. C. (1982). In *Computer Simulation of Solids* (eds. C. R. A. Catlow and W. C. Mackrodt). Springer-Verlag, Berlin, pp. 3–20.
- Carroll M. R. (1991) Diffusion of Ar in rhyolite, orthoclase and albite composition glasses. *Earth Planet. Sci. Lett.* **103**, 156–168.
- Carroll M. R., Sutton S. R., Rivers M. L. and Woolum D. S. (1993) An experimental study of krypton diffusion and solubility in silicate glasses. *Chem. Geol.* **109**, 9–28.
- Carroll M. R. and Draper D. S. (1994) Noble-gases as trace-elements in magnetic processes. *Chem. Geol.* **117**, 37–56.
- Chamorro E. M., Wartho J. A., Brooker R. A., Wood B. J., Kelley S. P. and Blundy J. D. (2002) Ar and K partitioning between clinopyroxene and silicate melt to 8 GPa. *Geochim. Cosmochim. Acta* **66**, 507–519.
- Cuadros F., Cachadiña I. and Ahumada W. (1996) Determination of Lennard-Jones interaction parameters using a new procedure. *Mol. Eng.* **6**, 319–325.
- Dick B. G. and Overhauser A. W. (1958) Theory of the dielectric constants of alkali halide crystals. *Phys. Rev.* **112**, 90–103.
- Ewald P. (1921) Die Berechnung optischer und elektrostatischer Gitterpotentiale. *Ann. Phys.* **64**, 253–287.
- Frenkel D. and Smit B. (2002) *Understanding Molecular Simulation From Algorithms to Applications*. Academic Press, New York.
- Gale J. D. (1997) GULP: a computer program for the symmetry-adapted simulation of solids. *J. Chem. Soc. Faraday Trans.* **93**, 629–637.
- Harper C. L. and Jacobsen S. B. (1996) Noble gases and earth's accretion. *Science* **273**, 1814–1818.
- Hayatsu A. and Waboso C. E. (1985) The solubility of rare-gases in silicate melts and implications for K–Ar dating. *Chem. Geol.* **52**, 97–102.
- Heber V. S., Brooker R. A., Kelley S. P. and Wood B. J. (2007) Crystal–melt partitioning of noble gases (helium, neon, argon, krypton, and xenon) for olivine and clinopyroxene. *Geochim. Cosmochim. Acta* **71**, 1041–1061.
- Hirschfelder J. O., Curtis C. F. and Bird R. B. (1964) *Molecular Theory of Gases and Liquids*. Wiley, New York.
- Hiyagon H. and Ozima M. (1986) Partition of noble gases between olivine and basalt melt. *Geochim. Cosmochim. Acta* **50**, 2045–2057.
- Honda M. and Patterson D. B. (1999) Systematic elemental fraction of mantle-derived helium, neon and argon in mid-oceanic ridge glasses. *Geochim. Cosmochim. Acta* **63**, 1874–2863.
- Jambon A., Weber H. and Braun O. (1986) Solubility of He, Ar, Kr and Xe in a basalt melt in the range 1250–1600 degrees. *Geochim. Cosmochim. Acta* **50**, 401–408.
- Jambon A. (1997) In *Volatiles in Magmas* (eds. M. R. Carroll and J. R. Holloway), p. 479.
- Lewis G. V. and Catlow C. R. A. (1985) Potential models for ionic oxides. *J. Phys. Solid State Phys.* **18**, 1149–1161.
- Lux G. (1987) The behaviour of noble-gases in silicate liquids–solution, diffusion, bubbles and surface effects, with applications to natural samples. *Geochim. Cosmochim. Acta* **51**, 1549–1560.
- Macedonia M. D., Moore D. D. and Maginn E. J. (2000) Adsorption studies of methane, ethane and argon in the zeolite mordenite: molecular simulations and experiments. *Langmuir* **16**, 3823–3834.
- Metropolis N., Rosenbluth A. W., Rosenbluth M. N., Teller A. H. and Teller E. (1953) Equation of state calculations by fast computing machines. *J. Chem. Phys.* **21**, 1087–1092.
- Miller G. W., Knaebel K. S. and Ikels K. G. (1987) Equilibration of nitrogen, oxygen, argon and air in molecular sieve 5A. *AIChE J.* **33**, 194–201.
- Mooij G. C. A. M., Frenkel D. and Smit B. (1992) Direct simulation of phase-equilibria of chain molecules. *J. Phys. Condens. Matter* **4**, L225–L259.
- Mott N. F. and Littleton M. T. (1938) Conduction in polar crystals. I. Electrolytic conduction in solid salts. *Trans. Faraday Soc.* **34**, 485–499.
- O'Nions R. K. and Oxburgh E. R. (1983) Heat and helium in the earth. *Nature* **306**, 429–431.
- Ozima M. and Igarashi G. T. (2000) The primordial noble gases in the Earth: a key constraint on Earth evolution models. *Earth Planet. Sci. Lett.* **176**, 219–232.
- Pellenq R. J. M. and Nicholson D. (1995) Grand ensemble Monte-Carlo simulation of simple molecules adsorbed in silicalite-1 zeolite. *Langmuir* **11**, 1626–1635.
- Purton J. A., Allan N. L., Blundy J. D. and Wasserman E. A. (1996) Isovalent trace element partitioning between minerals and melts: a computer simulation study. *Geochim. Cosmochim. Acta* **60**, 4977–4987.
- Purton J. A., Allan N. L. and Blundy J. D. (1997) Calculated solution energies of heterovalent cations in forsterite and diopside: implications for trace element partitioning. *Geochim. Cosmochim. Acta* **61**, 3927–3936.
- Roselieb K., Blanc P., Büttner H., Jambon A., Rammensee W., Rosenhauer M., Vielzeuf D. and Walter H. (1997) Experimental study of argon sorption in quartz: evidence for argon solubility. *Geochim. Cosmochim. Acta* **61**, 533–542.
- Sanders M. J., Leslie M. and Catlow C. R. A. (1984) Interatomic potentials for SiO<sub>2</sub>. *J. Chem. Soc. Chem. Commun.*, 1271–1273.
- Schlenker J. L., Pluth J. J. and Smith J. V. (1979) Positions of cations and molecules in zeolites with the mordenite-type framework VIII dehydrated sodium-exchanged mordenite. *Mat. Res. Bull.* **14**, 751–758.
- Seff K. and Shoemaker D. (1967) The structures of zeolite sorption complexes. I. The structures of dehydrated zeolite

- 5A and its iodine Sorption complex. *Acta Crystallogr.* **22**, 162–170.
- Shannon R. D. (1976) Revised effective ionic radii and systematic studies of interatomic distances in halides and chalcogenides. *Acta Crystallogr.* **A32**, 751–767.
- Shen D. (1991) Adsorption and frequency-response diffusion of sorbates in zeolites. PhD thesis, University of London.
- Shibata T., Takahashi E. and Ozima M. (1994). In *Noble Gas Geochemistry and Cosmochemistry* (ed. J. I. Matsuda). Terra Science Publishing, Tokyo, Japan, p. 43.
- Smit B. and Siepmann J. I. (1994) Computer simulations of the energetics and siting of *n*-alkanes in zeolites. *J. Phys. Chem.* **98**, 8442–8452.
- Taylor M. B., Barrera G. D., Allan N. L., Barron T. H. K. and Mackrodt W. C. (1997) Free energy of formation of defects in polar solids. *Faraday Discuss.* **106**, 377–387.
- Tschiyama A. and Kawamura K. (1994) Sites and behaviors of noble gas atoms in MgO crystal simulated by the molecular dynamics (MD) method. In *Noble Gas Geochemistry and Cosmochemistry* (ed. J. Matsuda). Terra Science Publishing, Tokyo, pp. 315–323.
- Turner G. (1989) The outgassing history of the Earth's atmosphere. *J. Geol. Soc. Lond.* **146**, 147–154.
- Van der Hilst R. D., Widiyantoro S. and Engdahl E. R. (1997) Evidence for deep mantle circulation from global tomography. *Nature* **386**, 578–584.
- Van Keken P. E. and Ballentine C. J. (1999) Dynamical models of mantle volatile evolution and the role of phase transitions and temperature-dependent rheology. *J. Geophys. Res.* **104**, 7137–7151.
- Van Koningsveld H., Van Bekkum H. and Jansen J. C. (1987) On the location and disorder of the tetrapropylammonium (TPA) ion in zeolite ZSM-5 with improved framework accuracy. *Acta Crystallogr.* **B43**, 127–132.
- Van Westrenen W., Allan N. L., Blundy J. D., Purton J. A. and Wood B. J. (2000) Atomistic simulation of trace element incorporation into garnets—comparison with experimental garnet–melt partitioning data. *Geochim. Cosmochim. Acta* **64**, 1629–1639.
- Vlugt T. J. H., Krishna R. and Smit B. (1999) Molecular simulations of adsorption isotherms for linear and branched alkanes and their mixtures in silicate. *J. Phys. Chem. B* **103**, 1102–1118.
- Wartho J.-A., Kelley S. P., Brooker R. A., Carroll M. R., Villa I. M. and Lee M. R. (1999) Direct measurement of argon diffusion profiles in a gem-quality Madagascar K-feldspar using the Ultra-Violet Laser Ablation Micro-probe (UVLAMP). *Earth Planet. Sci. Lett.* **170**, 141–153.
- Watanabe K., Austin N. and Stapleton M. R. (1995) Investigation of the air separation properties of zeolites type-A and type-X and type-Y by Monte-Carlo simulations. *Molecular Simulat.* **15**, 197.
- Wood B. J. and Blundy J. D. (2001) The effect of cation charge on crystal–melt partitioning of trace elements. *Earth Planet. Sci. Lett.* **188**, 59–71.
- Zhang Y. and Xu Z. (1995) Atomic radii of noble gas elements in condensed phases. *Am. Mineral.* **80**, 670–675.

Associate editor: James Kubicki